Title
Coupled supercritical CO2 dissolution and water flow in pore-scale micromodels

Authors
Chang, Chun
Zhou, Quanlin
Kneafsey, Timothy J
et al.

Publication Date
2019

DOI
10.1016/j.advwatres.2018.11.004

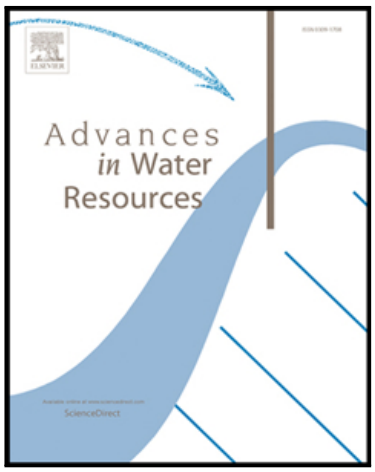

Coupled Supercritical CO_2 Dissolution and Water Flow in Pore-Scale Micromodels

Chun Chang , Quanlin Zhou , Timothy J. Kneafsey , Mart Oostrom , Yang Ju

PII: S0309-1708(18)30573-6
DOI: https://doi.org/10.1016/j.advwatres.2018.11.004
Reference: ADWR 3240

To appear in: *Advances in Water Resources*

Received date: 4 July 2018
Revised date: 4 November 2018
Accepted date: 14 November 2018

Please cite this article as: Chun Chang , Quanlin Zhou , Timothy J. Kneafsey , Mart Oostrom , Yang Ju , Coupled Supercritical CO_2 Dissolution and Water Flow in Pore-Scale Micromodels, *Advances in Water Resources* (2018), doi: https://doi.org/10.1016/j.advwatres.2018.11.004

Highlights

- Imbibition and supercritical CO_2 dissolution experiments were conducted in four micromodels possessing different pore-scale characteristics.
- We present the fundamental process of the non-equilibrium CO_2 dissolution and coupling with water flow.
- We investigate the impacts of pore characteristics on the coupled processes.
- A diagram is proposed to quantify the equilibrium/non-equilibrium dissolution transition and network-dependent coupled processes.

Coupled Supercritical CO_2 Dissolution and Water Flow in Pore-Scale Micromodels

Chun Chang [1, 2,*], Quanlin Zhou[2], Timothy J. Kneafsey[2], Mart Oostrom[3], Yang Ju[1, 4]

[1] State Key Laboratory of Coal Resources and Safe Mining, China University of Mining & Technology (Beijing), Beijing 100083, China

[2] Energy Geosciences Division, Lawrence Berkeley National Laboratory, University of California, Berkeley, California, CA94720, USA.

[3] Energy and Environment Directorate, Pacific Northwest National Laboratory, 902 Battelle Boulevard, P.O. Box 999, MSIN K8-96, Richland, Washington 99352, USA. Now at INTERA, Inc, Richland, WA.

[4]State Key Laboratory for Geomechanics and Deep Underground Engineering, China University of Mining & Technology, No 1, University Avenue, Xuzhou 221006, P. R. China

[*]Corresponding author. *E-mail address*: chunchang@lbl.gov

Abstract: Dissolution trapping is one of the most important mechanisms for geological carbon storage (GCS). Recent laboratory and field experiments have shown non-equilibrium dissolution of supercritical CO_2 ($scCO_2$) and coupled $scCO_2$ dissolution and water flow, i.e., $scCO_2$ dissolution at local pores/pore throats creating new water-flow paths, which in turn enhance dissolution by increased advection and interfacial area. However, the impacts of pore-scale characteristics on these coupled processes have not been investigated. In this study, imbibition and dissolution experiments were conducted under 40 °C and 9 MPa using a homogeneous/isotropic hexagonal micromodel, two homogeneous elliptical micromodels with low or high anisotropy, and a heterogeneous sandstone-analog micromodel. The four micromodels, initially saturated with deionized (DI)-water, were drained by injecting $scCO_2$ to establish a stable $scCO_2$ saturation. DI water was then injected at different rates with $logC_a$ (the capillary number) ranging from −6.56 to −4.34. Results show that bypass of $scCO_2$ by displacing water is the dominant mechanism contributing to the residual CO_2 trapping, triggered by heterogeneity in pore characteristics or pore-scale $scCO_2$-water distribution. Bypass can be enhanced by pore heterogeneity or reduced by increasing transverse permeability, resulting in relatively low (<2% of CO_2 solubility) or high (9 to 13% of CO_2 solubility) dissolved CO_2 concentration in displacing water. The overall dissolution of residual $scCO_2$ increases with decreasing C_a, and approaches to their solubility at low C_a value with sufficient residence time. This main trend is similar to a capillary desaturation curve that represents the relationship between the residual saturation and C_a. Spatially, dissolution initiates

along the boundary of bypassed $scCO_2$ cluster(s) in a non-equilibrium manner, and the coupling of water flow and dissolution occurs which fragments the bypassed $scCO_2$ clusters and enhance $scCO_2$ dissolution.

Keywords: Geological carbon storage, Micromodel, Pore characteristics, Imbibition, CO_2 dissolution, Mass transfer

1. Introduction

Accurate prediction of the long-term storage of CO_2 in subsurface formations depends largely on our understanding of involved processes, such as (1) two-phase fluid displacement and residual CO_2 saturation, and (2) dissolution of injected supercritical CO_2 ($scCO_2$) and mass transfer of dissolved CO_2 ($dsCO_2$) in formation brine (IPCC, 2005). The field tests of $scCO_2$ dissolution at the CO_2CRC Otway site (Haese et al., 2013; Paterson et al., 2013) have shown unexpectedly early breakthrough and low maximum $dsCO_2$ concentrations (~30% of CO_2 solubility) in the produced water that were credited to formation heterogeneity, indicating the non-equilibrium $scCO_2$ dissolution and mass transfer at the field scale. At the core scale, Berg et al. (2013) conducted imbibition and $scCO_2$ dissolution experiments in a homogeneous high-permeability (380 mD) Berea sandstone core at 10 MPa and 45 °C by injecting $dsCO_2$-undersaturated brine at 0.25 mL/min into the core after $scCO_2$ drainage. They observed strong dissolution of residual $scCO_2$ into displacing brine with relatively high $dsCO_2$ concentration (60% of CO_2 solubility). In contrast, Chang et al. (2013, 2014) observed that the complete, post-imbibition depletion of residual $scCO_2$ via dissolution was a prolonged process when injecting deionized (DI)-water free of $dsCO_2$ at 1.0 mL/min into two heterogeneous and low-permeability (<1 mD) sandstone cores at 8 MPa and 40 °C. The average $dsCO_2$ concentration was measured as 5% of CO_2 solubility, one order of magnitude lower than that in Berg et al. (2013). At the pore scale, Chang et al. (2016) investigated $scCO_2$ dissolution and mass transfer during imbibition in a heterogeneous sandstone-analog micromodel,

fabricated from section micrographs of a low-permeability Mt. Simon sandstone core (Zuo et al., 2013). Their time-lapse images of $scCO_2$-water distributions provide direct observations of the non-equilibrium CO_2 dissolution and mass transfer, caused by bypass of residual $scCO_2$ by displacing water after imbibition, and slow mass transfer of $dsCO_2$ to displacing water. The inferred $dsCO_2$ concentrations in this centimeter-scale micromodel ranged from 0.38% to 2.72% of CO_2 solubility. The disparate observations in $dsCO_2$ concentrations across these scales indicate that the effects of formation heterogeneity and pore-scale characteristics on $scCO_2$ dissolution and mass transfer need to be investigated.

Laboratory experiments have also shown coupled $scCO_2$ dissolution and water flow, i.e., $scCO_2$ dissolution at local pores/pore throats creating new water-flow paths, which in turn enhance dissolution by increased advection and interfacial area. At the core scale, Akbarabadi and Piri (2013) observed an increase in brine relative permeability caused by gradual reduction in the blockage by trapped $scCO_2$ bubbles via dissolution. At the pore scale, Buchgraber et al. (2012) showed the disconnecting and shrinking of CO_2 bubbles due to dissolution, indicating $scCO_2$ snap-off and residual trapping. The disconnection and shrinkage of the CO_2 phase, in return, enhances CO_2 dissolution and mass transfer by increasing CO_2-water interfacial area and creating new water-flow paths (Chang et al., 2016). Nambi and Powers (2000) and Zhang et al. (2002) reported similar coupled processes for the dissolution of non-aqueous phase liquid (NAPL) in water in heterogeneous sand boxes and columns packed with angular silica sands. Alternately, Chomsurin and Werth (2003) showed

constant NAPL dissolution rate with decreasing NAPL saturation during their imbibition experiments in 2D homogeneous and heterogeneous micromodels. Addressing the apparently contradictory observations requires a systematic study on the impacts of pore characteristics on trapping mechanism and dissolution of residual CO_2.

When gravitational forces are negligible, the nature of two-phase displacement at the pore scale has been characterized by the dimensionless capillary number C_a that represents the relative effect of viscous forces versus capillary force, and by the viscosity ratio *M* between liquid phases. The C_a is often defined as follows,

$$C_a = (\mu \times \overline{u})/(\sigma \times cos\theta) \qquad \text{Eq. (1)}$$

where μ is the viscosity, $\overline{u}$ the average Darcy velocity of the injected fluid, σ the interfacial tension, and θ the contact angle between the injected and resident fluid (Lenormand, et al., 1988). The phase entrapment at a given C_a and M can be described by the Capillary Desaturation Curve (CDC), which represents the relationship between the residual non-wetting saturation and C_a (Sahimi, 1993; Castro et al., 2015). The pore-scale CDC has been investigated in a micromodel with a statistically generated pore-size distribution (Castro et al., 2015). Their results suggest the dependence of CDC shape on the amount and size distribution of the residual phase. It has also been reported that the traditional C_a in Eq. (1) should be revised using the length scales corresponding to the size of non-wetting phase clusters, and the revised C_a is referred to as cluster-based C_a (Hilfer and Oren, 1996; Armstrong et al., 2014). The influence of pore characteristics on pore-scale CDC and

cluster-based C_a for residual trapping and the later dissolution of residual CO_2 needs further investigations.

In this study, we (1) present the fundamental trapping mechanism and the processes of the non-equilibrium CO_2 dissolution coupled with water flow, (2) investigate the impacts of pore characteristics on CO_2 trapping, the pore-scale CDC and the coupled processes, and (3) propose a diagram to quantify the network-dependent coupled processes. A series of imbibition and $scCO_2$ dissolution experiments was systematically conducted in four micromodels with post-drainage $scCO_2$ saturations by injecting $dsCO_2$-free brine at different rates. Time-lapse high-resolution images of $scCO_2$ and water were obtained to provide direct observations of the coupled processes at the pore scale and to allow for comparisons among the different micromodels and with previous studies at the pore and core scales. The four micromodels represent typical pore characteristics of porous media with contrasts between homogeneity and heterogeneity, between isotropy and weak and strong anisotropy, and between different pore shapes.

We first present the details on the micromodels and experimental procedures in Section 2. We show in Section 3 the fundamental processes of CO_2 dissolution coupled with water flow in a homogeneous isotropic micromodel at two low injection rates ($logC_a = -6.53$ and -6.13), and then the effects of displacement rate on CO_2 dissolution. In Section 4, we discuss the impacts of pore characteristics on the coupled processes by comparing the experimental observations in all the four micromodels. In Section 5, we present the pore-scale CDC and cluster-based C_a in different

micromodels. In Section 6, we propose a diagram to describe the network-dependent coupled processes and the overall trend between dsCO$_2$ concentration and C_a or water residence time. We conclude our observations and include implications on field GCS in Section 7.

2. Materials and methods

2.1 Micromodels

Figure 1 shows the pore characteristics of the four micromodels used in this study, with pore space shown in white and silicon posts (representing mineral grains) in black. Micromodels were composed of etched silicon wafers fabricated using micro-fabrication methods involving standard photolithography, coupled plasma-deep reactive ion etching (ICP-DRIE), thermal oxidation, and anodic bonding (Chomsurin and Werth, 2003; Willingham et al., 2008). Micromodel #1 consists of hexagonal posts and a homogeneous isotropic pore network, with circular pore bodies (60 μm in diameter), each connected with six pore throats (5 μm in width). Micromodels #2 and #3 are homogeneous anisotropic micromodels, share the same elliptical silicon posts, and have different post arrangements and thus different longitudinal (k_l) and transverse (k_t) permeability. The ratio of k_t/k_l is calculated as 0.63 for Micromodel #2 and 6.86 for Micromodel #3, using the relation $k = \frac{1}{2}\left(\frac{A}{P}\right)^2$, where A and P represent the area and perimeter of a rectangular cross section, respectively (White, 1979). The design pore depth of the three micromodels is 37 μm. The pore network of Micromodel #4 is extracted from a section micrograph of a Mt. Simon sandstone core

collected from the injection well of the Illinois Basin-Decatur project (Zuo et al., 2013; Senel et al., 2014). The porous medium portion consists of nine identical sub-images in a 3×3 array (see the red lines in Figure 1) and features in three lateral high-permeability channels (see Figure S1 in the supplementary information). A Local Thickness plugin in ImageJ software (Hildebrand and Rüesgsegger, 1996; Rasband, 1997-2018) was used to quantify the pore-size distribution shown in Figure S1. The average pore-body diameter and pore-throat width is 33 and 14 μm, respectively. Figure S1 presents an example of the micromodel design including the pore network (#4) and the boundary conditions (Zuo et al., 2013). The triangle sections on each side of the pore allow for an uniform water displacement before entering the pore network (see Figure S3), reducing water film flow before invading the pore network. The inlet triangle volume was included when calculating the water injection pore volume (PV). Additional details on the pore-size distribution can be obtained from Chang et al. (2016). Table 1 lists the properties of the four micromodels used in this study.

2.2 Experiments and fluorescence imaging

An experimental setup with four high-pressure syringe pumps (Teledyne ISCO Inc., Lincoln, NE) was used for all imbibition/dissolution experiments. The experimental setup is described in detail in the supplementary figure (Figure S2). Each micromodel was assembled against a sapphire viewing window in a high-pressure cell allowing imaging. The micromodel was initially saturated with deionized (DI)-water, and then drained by injecting Coumarin-dyed $scCO_2$ (Biswas et

al., 1999) at a constant rate until stable $scCO_2$ distribution and saturation were established. The displaced water during drainage was collected in a pressure pump maintaining back-pressure at a constant fluid pressure of 9.00 MPa. After $scCO_2$ distribution and saturation remained stable with time, the $scCO_2$ distribution was imaged to calculate the baseline $scCO_2$ saturation. The same drainage procedure was repeated before each imbibition/dissolution experiment to obtain similar initial $scCO_2$ saturation ($S_{g,i}$) and distribution.

Imbibition/dissolution experiments were conducted by injecting DI water at a constant volumetric rate until $scCO_2$ in the pore network was completely depleted. Displaced $scCO_2$ was collected in the back-pressure pump constantly maintained at 9.00 MPa. Different water injection rates were used for each micromodel (see Table 2). To allow for comparisons between imbibition/dissolution experiments and micromodels, we calculated the capillary number (C_a) for each test from Eq. (1). The reported contact angle of water–Courmarin dyed $scCO_2$ in micromodels fabricated using similar silicon wafers is approximately 15° (Wang et al., 2012). σ is inferred from Chiquet et al. (2007) for $scCO_2$ and water.

During each imbibition/dissolution experiment, the stained $scCO_2$ in the micromodel was observed through a Blue GFP filter set (λ_{ex} = 379-401 nm, λ_{em} = 435-485 nm). Time-lapse images were obtained using a Nikon Eclipse TE2000-E epifluorescent inverted microscope (Melville, NY) equipped with a monochrome CCD camera (MU1003, AmScope) through a 4X objective with a spatial resolution of 1.62 μm/pixel. During the experiment, images were taken at 2-40 min intervals,

depending on the water injection rates and durations. The fluorescent signal intensity of dyed $scCO_2$ is significantly higher than that for silicon posts and pore spaces filled with water, with signal-to-noise ratio > 10. A threshold value was unambiguously determined for each image to distinguish the $scCO_2$ phase from others following methods outlined by Zhang et al. (2011) and Chang et al. (2016). Segmentation and analysis of these images were conducted using ImageJ software (Rasband, 1997-2018). The image segmentation method was validated by comparing (1) the measured porosity from fluorescent images to that computed from the micromodel design and (2) the measured size of silicon posts to the design value. Both of the comparisons showed good agreement with errors <5%. For Micromodel #3, images taken at a resolution of 1.62 μm/pixel failed to capture the very tight pore throat with 3 μm width (see Figure 1), leading to an error in image segmentation and underestimation of the pore volume by <2.5%. CO_2 distributions were assumed to be uniform along the micromodel depth for the calculation of CO_2 saturations. This assumption has been widely used for 2D micromodel experiments (Zhang et al., 2011; Wang et al., 2013; Chang et al., 2017; Hu et al., 2017).

3. CO_2 imbibition and dissolution processes

A series of imbibition/dissolution experiments was conducted in the homogeneous and isotropic Micromodel #1 under different displacement rates varying from 10 to 200 μL/h ($logC_a = -6.53$ to -5.23). During each experiment, time-lapse images of $scCO_2$ distribution were obtained to calculate a $scCO_2$ saturation and depletion rate (Q_d).

3.1 Imbibition and residual CO_2 saturation

Figure 2a shows selected time-lapse images of $scCO_2$ distribution (green) obtained during the imbibition/dissolution experiment with $logC_a = -6.53$. Water (dark) invades the pore network in several narrow (with 1-2 pore bodies wide) and long flow paths, and flows through the pore network within 2 min. Initially, the residual water clusters near the inlet help induce channelized water flow (see the white arrows at 0 and 5.6 PV in Figure 2a). The channelized water flow results in a high residual $scCO_2$ saturation ($S_{g,r}$) of 0.82 (see Figure 2a at 6.4 PV injection and Table 3), with the majority of injected water flowing through water-flow channels and bypassing the rest of the pore network. Similar channelized water flow is observed in the imbibition/dissolution experiment with $logC_a = -6.13$ (see Figure 2b). Five narrow water-flow paths (at 1-2 pore width), labeled as C1, C2, C3, C4 and C5, have been created by 2.4 PV (22 min) after the start of water injection. The residual CO_2 saturation at the end of imbibition, when no additional CO_2 was displaced from the pore-network, is 0.79 (also see Table 3).

In this homogeneous micromodel, the bypass of $scCO_2$ by displacing water can be attributed to the initially heterogeneous fluid distribution near the inlet. Similar bypass trapping of residual CO_2 has been observed in a homogeneous micromodel (Hu et al., 2017) and a glass beads column (Chaudhary et al., 2013). At C_a>10^{-7}, the main trapping mechanism was shown by the propagation of invading fluid fingers that lead to clusters of defending fluid being bypassed (Hu et al., 2017).

3.2 Coupled CO_2 dissolution and water flow

After imbibition, $scCO_2$ dissolution and mass transfer are dominant mechanisms for $scCO_2$ depletion with time. In the case with $logC_a = -6.53$, a low-tortuosity flow path connected to the outlet gradually develops as the main water-flow path, and its width continuously increases with $scCO_2$ dissolution until the complete depletion of residual $scCO_2$ (see Figure 2a). Figures 3a-b show the temporal CO_2 saturation averaged over the pore network and effluent $dsCO_2$ concentration at the micromodel outlet as a function of water injection time or pore volume (PV) during the experiment, while Figure 3c shows the dependence of $scCO_2$ depletion rate (g/PV) on $scCO_2$ saturation. The rate of $scCO_2$ depletion is defined as the depleted $scCO_2$ mass (g) per PV and calculated from two consecutive images. The $dsCO_2$ concentration is calculated as follows on the basis of mass balance assuming that dissolution and water advection are solely responsible for the $scCO_2$ depletion after the imbibition is complete:

$$C = \frac{\rho P(S_{t2} - S_{t1})}{MQ(t_2 - t_1)} \quad \text{Eq. (2)}$$

Here C is the dissolved CO_2 concentration (mol/L), ρ is CO_2 density under experimental conditions (g/mL), P is pore volume of the porous network (mL), S_{t2} and S_{t1} indicates CO_2 saturation at two sequential images, t represents water injection time (min), Q is the water injection rate (L/min) and M (44 g/mol) refers to the CO_2 molar mass. Note that $scCO_2$ saturation, $dsCO_2$ concentration, and $scCO_2$ depletion rate are average values over the entire pore-network domain, if not otherwise specified. The assumption that dissolution and water advection are solely responsible for the $scCO_2$ depletion after the imbibition is made carefully by

substantial evidence showing no displacement of CO_2 occur after the completion of imbibition, i.e., the CO_2 bubbles/clusters at the outlet triangle void shrink due to dissolution and no additional CO_2 displaced out from the pore-network was seen (see Figure S3). The evaporation of water in $scCO_2$ was negligible when calculating the CO_2 depletion. Under the experimental conditions (40 °C, 9 MPa), the solubility of water in $scCO_2$ is ~3.5×10^{-3} (mole fraction), while the solubility of $scCO_2$ dissolved in water is 22×10^{-3} in mole fraction (Spycher and Pruess, 2003). Meanwhile, the dissolution and mass transfer of $scCO_2$ in water are enhanced by water advection, while evaporation of water in $scCO_2$ is diffusion dominated in the stagnant CO_2. Evaporation of water in $scCO_2$ thus has a limited effect on the $scCO_2$ depletion rate after imbibition.

As shown in Figure 3a, it takes 2,010 min to complete the depletion of $scCO_2$ by imbibition (150 min or 6 PV) and dissolution (1,860 min or 80 PV). The rate of $scCO_2$ depletion by dissolution (with initial $scCO_2$ saturation of 0.82) varies from 1.67×10^{-6} to 4.72×10^{-5} g/PV, and corresponds to an effluent $dsCO_2$ concentration of 0.82-22.4% of CO_2 solubility (C_s=1.225 mol/L) under the experimental conditions (Spycher and Pruess, 2003). In contrast, under equilibrium dissolution assumption, 6.7 PV of injected water is needed to completely dissolve the residual CO_2 in the pore network, corresponding to 97 min at the 10 μL/h (0.069 PV/min) water injection rate.

The coupled $scCO_2$ dissolution and water flow can be first understood by the non-monotonic temporal change in $scCO_2$ depletion rate, i.e., $scCO_2$ depletion rate increases first from 0.2×10^{-5} g/PV to 4.7×10^{-5} g/PV first with decreasing $scCO_2$

saturation in the pore network from 0.80 until a certain value (0.45 in Figure 3c), after which the rate decreases. This trend is also seen in Figure 3b for dsCO_2 concentration. To improve understanding of the coupled processes, we depict in Figure 4 the fraction and location of scCO_2 mass dissolved within different time intervals in the micromodel at $logC_a = -6.53$, with different colors corresponding to different injection times and PVs. Along the boundary layers (marked by white dotted lines) of the two bypassed scCO_2 clusters separated by the single water-flow path, water flow develops in local pores/pore clusters and breaks large connected scCO_2 clusters by dissolution (see the white arrows – cooler colors in warmer color regions). The local water-flow paths developed by scCO_2 dissolution greatly increase the average dsCO_2 concentration in the entire pore network from 0.82% to 22.4% of CO_2 solubility. The increased scCO_2 dissolution rate by coupled dissolution and water flow is similar to that observed experimentally by Zhang et al. (2002) and Chang et al. (2016) and verified numerically by Zhao et al. (2003). At later times, this coupling of scCO_2 dissolution and water flow is weakened due to the reduced residual CO_2 mass available for dissolution. The overall dsCO_2 concentration vs. water injection volume and CO_2 depletion rate vs. CO_2 saturation thus shows a maximum value.

The coupling between scCO_2 dissolution and water flow can be further understood by the multiple water-flow paths and their competition in the case with $logC_a = -6.13$. As shown in Figure 2b, flow paths #C2, #C3 and #C4 increases in their width simultaneously during the first 214 min. After that, all injected water migrates through flow path #C2 and its width increases with time until the complete depletion of

residual $scCO_2$. Figure 5a-c shows magnified local regions with 30 pores wide along each flow path to show the competition between flow paths #C2 through #C4, and in Figure 5d shows the temporal saturation change during the first 244 min (17 PV). For #C2, upstream $scCO_2$ dissolves into the displacing water along the flow path, and $scCO_2$ saturation decreases almost linearly with time from 0.81 to 0.74, indicating a relatively constant $scCO_2$ dissolution rate. Along #C3, however, $scCO_2$ saturation decreases nonlinearly with time from 0.72 to 0.68 with a decreasing CO_2 dissolution rate. The stable $scCO_2$ bubbles within the narrow flow path (marked by the red arrow in Figure 5b) may indicate high, local $dsCO_2$ concentration close to solubility. In #C4, as $scCO_2$ dissolves in the upstream water, a large $scCO_2$ cluster is displaced and blocked the narrow flow path downstream. This local displacement terminates the water flow and reduces CO_2 depletion rate. After 214 min, #C3 and #C4 are suppressed, and #C2 dominates further $scCO_2$ depletion in the entire pore network (see Figure 2b). For #C1 and #C5, the water flow paths are not connected to the micromodel outlet after imbibition, resulting in a constant CO_2 saturation as shown in Figure 5d.

Figures 3d and e show the temporal network-averaged CO_2 saturation and effluent $dsCO_2$ concentration as functions of water injection time or volume for the case with $logC_a = -6.13$, while Figure 3f shows the dependence of $scCO_2$ depletion rate on $scCO_2$ saturation. The $scCO_2$ depletion rate increases from 4.0×10^{-6} to 1.9×10^{-5} g/PV and the corresponding $dsCO_2$ concentration varies from 1.88 to 8.98% of CO_2 solubility. Figure 6 depicts the fraction and location of $scCO_2$ mass dissolved at

different injection times and volumes, indicating that the coupled $scCO_2$ dissolution and water flow occur in the boundary layers of bypassed $scCO_2$ clusters. As shown in the figure, the main water flow path (C2) is less tortuous than that in Figure 4, and the coupled water flow and dissolution is less pronounced with reduced transverse water flow into the bypassed $scCO_2$ clusters.

An additional imbibition experiment without dissolution was conducted by injecting $dsCO_2$-saturated water at $logC_a = -6.13$. Figure 7 shows the time-lapse images and tortuous water-flow paths. The residual $scCO_2$ saturation after imbibition (without dissolution) is 0.72. The tortuous flow paths are compared to the five straight ones in Figure 2b. This indicates that dissolution can lead to $scCO_2$ displacement in more focused, less tortuous, narrower flow paths with reduced sweep efficiency. The depletion of $scCO_2$ by dissolution at local pores may enhance water flow development and reduce resistance from $scCO_2$ within the flow path. Similar observations have been presented by Chang et al. (2016).

3.3 Effects of water velocity on imbibition and dissolution

The velocity effects on imbibition and dissolution were investigated by increasing water injection rates in the imbibition/dissolution experiments conducted in Micromodel #1. Figure 8 shows the time-lapse images of $scCO_2$-water distribution in the cases with $logC_a = -5.83$, -5.53 and -5.23. Injected water displaces $scCO_2$ in randomly distributed forward and lateral flow paths (i.e., in the form of a dendritic front), leaving small $scCO_2$ clusters entrapped. Sweep efficiency is greatly increased with increasing displacement rates, resulting in larger number and width of the

invading water flow paths, resulting in residual $scCO_2$ saturation (at the end of imbibition) at 0.57, 0.58 and 0.47 for $logC_a = -5.83$, -5.53 and -5.23, respectively (see Table 3). The imbibition characteristics appears to transit from channelized water flow observed in the two low flow rate cases with $logC_a = -6.53$ and -6.13 to dendritic displacement in the higher-rate cases.

The transition of water-flow regimes (from channeling flow to dendritic displacement) shown in Figures 2 and 8 may also be attributed to the high pore-throat aspect ratio (12) of Micromodel #1 and increased viscous force with injection rates. This transition observed experimentally in this study is similar to that obtained by pore-scale modeling with different flow rates and pore-throat aspect ratios conducted by Hughes and Blunt (2000). They found channelized water flow in the case with a small water injection rate ($logC_a = -6.0$) and a high pore-throat aspect ratio (3.95) and dendritic displacement in the cases with higher injection rates ($logC_a > -6.0$) and both high and low pore-throat aspect ratio (3.95 and 2.1).

The rate-dependent imbibition characteristics considerably impact the subsequent $scCO_2$ dissolution and mass transfer. Figure 9 shows the depletion of the residual $scCO_2$ by dissolution at different time and water injection volumes for the three high-rate experiments. After imbibition, small isolated $scCO_2$ clusters within the water-flow paths dissolve first, followed by the larger bypassed clusters. The coupled dissolution and local water flow (marked by the white arrows in Figure 9) occur and enhance $scCO_2$ dissolution in the pore network. Figure 10 shows the comparison of the time-dependent $scCO_2$ saturation, $dsCO_2$ concentration, and $scCO_2$ depletion rate

among the five experiments with $logC_a$ from −6.53 to −5.23 conducted in Micromodel #1. The $scCO_2$ depletion time after imbibition is 1860, 1272, 557, 235, and 122 min, respectively (see Table 3), indicating the effect of flow rate on the $scCO_2$ residual saturation and the enhanced dissolution with flow rate. In contrast, it would take 97, 40, 14, 7 and 3 min for equilibrium dissolution to completely deplete residual $scCO_2$ in the corresponding experiment. The prolonged depletion time indicates non-equilibrium $dsCO_2$ dissolution in the homogeneous pore network caused by (1) non-uniform $scCO_2$-water distribution after imbibition and (2) non-uniform water-flow paths during dissolution. The depletion time mainly depends on the dissolution rate of large $scCO_2$ clusters surrounded by water-carrying flow paths, even though enhanced dissolution can be caused by additional, local or global, water-flow paths.

Figure 10b displays that the peak $dsCO_2$ concentration (caused by coupled dissolution and water flow) decreases with increasing imbibition rates (larger C_a). These rate-dependent coupled processes can be attributed to the residence time of injected water in the pore network. Longer residence time with lower imbibition rates allows for longer contact between $scCO_2$ and mobile water that is available for dissolution and mass transfer. In addition, because of the water-wet silica surface, water flow may occur as thin film along the surface of the silica posts (Zhao et al., 2016; Zacharoudiou et al., 2017; Hu et al., 2018). The swelling of water films was investigated as a slow diffusion process driven by capillary pressure at localities (Nguyen et al., 2006), i.e., with the increase in water injection rate, the time for

swelling of wetting films and development of local water flow is shortened. The coupling between dissolution and local water flow is thus limited, reducing the dsCO_2 concentration in the pore network. This indicates that water flow at a high velocity is less effective in dissolving residual scCO_2 than that at a slower velocity and equilibrium scCO_2 dissolution may only occur in regional groundwater flow with a very small (close to zero) velocity (to be further discussed in Section 5).

4. Effects of pore characteristics

Imbibition and dissolution experiments were conducted in Micromodels #2, #3 and #4 to improve understanding of the impacts of pore characteristics (i.e., anisotropy and heterogeneity) on CO_2 dissolution and its coupling with water flow.

4.1 Anisotropy with higher longitudinal permeability, k_t/k_l =0.63

In Micromodel #2 with higher longitudinal permeability (k_t/k_l=0.63), two imbibition and dissolution experiments were conducted by injecting water at 10 and 50 μL/h ($logC_a$= −6.56 and −5.86). Due to the higher longitudinal permeability, both drainage and imbibition efficiencies are reduced compared to Micromodel #1. After drainage, scCO_2 saturations are ~0.50 for subsequent imbibition experiments. Figures 11a and b show selected temporal images of scCO_2-water distribution during the two experiments. Water invades the pore network from left boundary in narrow flow channels (marked by white dotted lines) with reduced displacement efficiency, leading to residual scCO_2 saturation of 0.43 and 0.44 after imbibition.

Figure 11c-e show the temporal CO_2 saturation, dsCO_2 concentration, and scCO_2 depletion rate. The residual CO_2 was completely depleted after water injections at 1300 and 275 min, corresponding to 55 and 60 PV (see Figure S4a), respectively, with $logC_a$= −6.56 and −5.86. The CO_2 depletion rate increases with decreasing scCO_2 saturation (Figure 11e) and the dsCO_2 concentration increases with water injection volumes (Figure 11d), indicating the coupling of CO_2 dissolution with water flow. The coupling occurs when water-flow paths merge with stagnant water clusters (see the white arrows in Figure 11a) and several flow paths merge into a large one (see the white arrows in Figure 11b).

4.2 Anisotropy with higher transverse permeability, k_t/k_l =6.86

Two imbibition/dissolution experiments were conducted in Micromodel #3 with a higher transverse permeability ($k_t/k_l = 6.86$) by injecting water at 10 and 50 µL/h ($logC_a$= −6.27 and −5.58). Under these conditions, both drainage and imbibition efficiency is high compared to Micromodels #1 and #2. scCO_2 saturation is stable at ~0.90 after drainage and injected water invades widely, distributed over the entire pore network (see Figure 12a and b). The displaced CO_2 saturation is 0.38 and 0.49, respectively, resulting in residual CO_2 saturation at 0.52 and 0.44 after imbibition (see Table 3).

The temporal change in CO_2 saturation is shown in Figure 12c. It takes 320 min (19 PV) and 90 min (27 PV) to completely deplete the scCO_2 by imbibition and dissolution at $logC_a$= −6.27 and −5.58, respectively (see Figure S4b for the change of CO_2 saturation vs. injected water pore volumes). The depletion of residual scCO_2

by dissolution starts after 40 min (5 PV) and 20 min (13 PV) and the dsCO_2 concentration monotonically decreases with increased water injection volumes (see Figure 12d). A monotonic decrease is also observed for the temporal change in CO_2 depletion rate (Figure 12e). The fast depletion and high dsCO_2 concentration by dissolution in these two experiments can be attributed to the strong water-film flow driven by high capillary pressure in the very tight pores and pore throats in Micromodel #3. The distributed contact between scCO_2 and mobile water is pervasive through the entire pore network, promoting scCO_2 dissolution everywhere. No dominant water-flow paths are observed.

4.3 Sandstone-analog heterogeneity

A series of imbibition and dissolution experiments were conducted in (heterogeneous sandstone-analog) Micromodel #4 and reported in Chang et al. (2016). Time-lapse images of scCO_2-water distribution show water preferential water flow along the high-permeability channels and bypass the majority of pore-network domain, where CO_2 was trapped and residual water after drainage was stagnant (see Figure 13). The results of dynamic dsCO_2 concentration vs. water injection show that scCO_2 dissolution at the pore-network scale is controlled by (1) the number of water-flow paths developed along the high-permeability channels, and (2) the velocity of water flow or dissolution time. At a low injection rate ($logC_a = -5.34$), one water-flow path develops with strong coupling between dissolution and water flow. With increasing in water injection rate ($logC_a = -4.34$), 2-3 water-flow paths develop along the high-permeability channels, while the coupling between dissolution and water flow is

diminished and dsCO_2 concentration decreases with water injection volumes. More details on the water flow and scCO_2 dissolution can be seen in Figures S5 and S6 in the supporting material and Chang et al., (2016). In summary, the coupling of dissolution with water flow in this heterogeneous micromodel depends largely on injection rate and capillary number.

5. Pore-scale capillary desaturation curve and cluster-based capillary number

Figure 14 shows the residual scCO_2 saturation and effluent dsCO_2 concentration as a function of C_a for the 13 imbibition and dissolution experiments in the four micromodels. The evolution of pore-scale residual CO_2 saturation follows a typical CDC for Micromodels #1 and #4, and the residual CO_2 saturations remain high at low C_a and decrease sharply at a critical C_a (marked by the arrows in Figure 14a). The residual CO_2 saturation in Micromodel #1 shows a reduction from 0.82 to 0.47, larger than that from 0.54 to 0.37 in Micromodel #4. Meanwhile, the residual CO_2 saturation decreases considerably at $logC_a = -5.83$ in Micromodel #1, while a great reduction occurs at $logC_a = -5.34$ in Micromodel #4. This indicates a higher viscous force is required for mobilizing the trapped CO_2 in the heterogeneous micromodel (#4). The pore heterogeneity tends to limit water flow in high-permeability channels and reduce viscous force to the bypassed CO_2. While the CDC for Micromodels #2 and #3 are not complete, residual CO_2 saturations in the two anisotropic micromodels are lower than in Micromodels #1 and #4 at similar C_a, caused by a lower drainage efficiency in Micromodel #2 and a higher imbibition efficiency in Micromodel #3 (see Tables 2

and 3).

As shown in Figure 14b, the $dsCO_2$ concentration generally decreases with increasing C_a, consistent with the CDC in Figure 13a. Under the same C_a, the $dsCO_2$ concentration increases with increasing water displacement efficiency from the lowest (<2% of CO_2 solubility) in Micromodel #4 to highest (9-13% of CO_2 solubility) in Micromodel #3. The $dsCO_2$ concentrations in Micromodels #1 and #2 range from 2 to 5% of CO_2 solubility.

The CDC shown in Figure 14a represents the pore-network-scale sweep efficiency as channelized water flow and bypass dominate the displacement. The bypassed pore-network domain may be composed of both trapped CO_2 ganglia and stagnant water (see Figure 13), which does not transfer viscous force or contribute to the mobilization of CO_2. Here, we calculate the cluster-based capillary number, $\overline{C_a}$, following Hilfer and Oren (1996):

$$\overline{C_a} = \frac{l^{cl}\mu\bar{u}}{kp_b} \qquad \text{Eq. (3)}$$

where l^{cl} is the average cluster length with saturation-weighting for each cluster:

$$l^{cl} = \frac{\sum s_c l_{cl}}{\sum S_c} \qquad \text{Eq. (4)}$$

l_{cl} represents the cluster size of the bypassed pore-network domain, instead of individual CO_2 ganglia from Hilfer and Oren (1996), k is the absolute brine permeability, and p_b is the capillary pressure at breakthrough, estimated from the pore size and depth of the micromodel:

$$p_b = \frac{\sigma cos\theta(r_1+r_2)}{r_1 r_2} \qquad \text{Eq. (5)}$$

In Eq. (5), σ =28 mN/m^2 (Chiquet et al., 2007), and for Micromodel #1, r_1= 60 μm, r_2=37 μm; for Micromodel #2, r_1= 106 μm, r_2=37 μm; For Micromodel #3, r_1= 41.6 μm, r_2=37 μm; For Micromodel #3, r_1= 33 μm, r_2=35 μm. The l^{cl} values for each imbibition/dissolution experiment are listed in Table 3.

Figure 14c displays CDC with $\overline{C_a}$. The desaturation of CO_2 occurs at $\overline{C_a}$ =0.52 and 1.69 in Micromodels #1 and #2, respectively. If individual CO_2 ganglia are used for calculating $\overline{C_a}$, the plot for Micromodel #4 shifts left by ~2 orders of magnitude. $\overline{C_a}$ may be modified further with measurements of relative permeability following Armstrong et al. (2014). We show here the uncertainty of determining the cluster size, and the important role of water flow regime. While the cluster-based capillary number provides new insights into the non-wetting phase mobilization when considering the system characteristics (both pore space and resident fluid), a broader application requires a better calculation of the size of the non-wetting phase clusters, especially when direct visualization and imaging are unavailable.

6. The relation between dsCO_2 concentration and $logC_a$

We've shown in Sections 3 and 4 that the bypass of scCO_2 by displacing water is the dominant mechanism contributing to residual CO_2 trapping without buoyancy. Bypass can be caused by the heterogeneity of pore characteristics (e.g., Micromodel #4) and pore-scale fluid distribution after drainage (e.g., Micromodels #1, #2 and #3). After imbibition, dissolution of residual CO_2 is dependent on the displacement rate and pore characteristics. In Figure 15a, we show the correlation of dsCO_2 concentration vs. Peclet number (*Pe*) for the imbibition/dissolution experiments

conducted in the four micromodels. The overall dsCO_2 concentrations decrease with increasing *Pe*, which can be attributed to (1) the decrease in residual CO_2 saturation after imbibition for dissolution, (2) the decrease in residence time, and (3) the reduced coupling between CO_2 dissolution and water flow. We also note the effects of pore characteristics on CO_2 dissolution and mass transfer. For instance, under the same range of *Pe* (0.3 to 17), dsCO_2 concentration is lowest in the heterogeneous micromodel because of the preferential water flow along the high-permeability channels (see Figure S5-6 for details). The value is highest in the strong anisotropic Micromodel #3 with higher transverse permeability (k_t/k_l=6.86), and 2 to 5% of solubility in homogeneous Micromodel #1 and weakly anisotropic Micromodel #2. The change of dsCO_2 concentration vs. Reynold number (Re) shows a similar trend (see Figure 15b and Table 2 and 3).

To improve understanding of the scCO_2 dissolution process for these experiments in particular, and other non-wetting phase fluids in general, we propose a diagram between the relative concentration of dissolved constituents and flow velocity in terms of $logC_a$. The diagram (Figure 16) includes (1) the average dsCO_2 concentration (solid symbol) and the range between maximum and minimum time-dependent concentrations (bar) in each dissolution experiment in this study, (2) the average and range of dsCO_2 concentration obtained in the core-flooding tests conducted in two low-permeability sandstone cores (Chang et al., 2014), (3) the average concentration obtained in a high-permeability Berea sandstone core (Berg et al., 2013), and (4) dissolved NAPL concentrations obtained in dissolution

experiments conducted in homogeneous and heterogeneous micromodels with $logC_a$= −6.80 and −6.0 (Chomsurin and Werth, 2003). The flow velocity, capillary number and Reynolds number in Berg et al. (2013) are 0.37 m/day, 9.3×10^{-8} and 1.06, while the values in Chang et al. (2014) are 0.73 m/day, 1.8×10^{-7} and 0.64. The relative concentration (in percentage) to the solubility of $scCO_2$ or NAPL under the experiment conditions is used in the diagram.

The overall trend shown in Figure 16 is that the dissolved non-wetting phase fluid concentration increases with a decrease in $logC_a$ (i.e., the increase in water residence time), and approaches to their solubility with sufficient residence time. In addition to the main trend, the relative dissolved phase concentration is also affected by the pore heterogeneity and anisotropy, and the coupled dissolution and water flow that depend on limited or pervasive water-flow paths in the regime of non-equilibrium dissolution. This effect can be understood by the wide range of relative concentration for a given $logC_a$ or water residence time. The average relative concentration varies from the lowest (<2%) in Micromodel #4, with strong heterogeneity, to the highest (9 to 13%) in Micromodel #3, with strong anisotropy. In Micromodels #1 and #2, with isotropic homogeneity and weak anisotropy, the concentration ranges from 2 to 5%. The lower relative concentration in the heterogeneous micromodel implies that for the same groundwater velocity, it may take longer residence time (or water flow path length) in a heterogeneous formation for $scCO_2$-water to reach equilibrium dissolution than that in a homogeneous one. Through the $dsCO_2$ concentration vs. CO_2 saturation observed in the four micromodels (Figures 11, 12 and 13), we are able to classify (1) Zone I,

where relative concentration monotonically decreases with decreasing residual saturation (marked by the red bars) and no coupling of CO_2 dissolution and water flow was observed, and (2) Zone II, where relative concentration non-monotonically changes with decreasing residual CO_2 saturation (marked by the black bars) and dissolution is coupled with water flow. Zones I and II are divided at a relative concentration of 5% (the dashed line) and $logC_a$ of -5.20. The dashed line for 2% concentration separates the dsCO_2 concentration in the heterogeneous micromodel from the other micromodels and cores. The proposed diagram helps describe the conditions that the coupled dissolution and water flow may occur at both pore scale with varying pore characteristics and core scale with varying porosities and permeabilities.

7. Conclusions and implications

We've systematically investigated the non-equilibrium CO_2 dissolution and its coupling with global and local water flow using four micromodels that represent porous media with varying anisotropy, heterogeneity, and pore-throat aspect ratio. Time-lapse images of scCO_2-water distributions were obtained during each imbibition and dissolution experiment to quantify the dynamic dissolution process.

In the four centimeter-scale micromodels and at imposed water velocities (resulting in $logC_a$=−6.56 to −4.34), we show that bypass of scCO_2 by displacing water is the dominant mechanism contributing to residual CO_2 trapping without buoyancy. Bypass can be triggered by heterogeneity in pore characteristics (e.g., Micromodel #4) and pore-scale scCO_2-water distribution (e.g., Micromodels #1 and

#2). Higher transverse permeability (e.g., Micromodel #3) may reduce the bypass and increase pore-network sweep efficiency. After imbibition, dissolution dominates the depletion of residual CO_2. We show the dissolved CO_2 concentration increases with increasing water displacement efficiency under same rates from the lowest (<2% of CO_2 solubility) in Micromodel #4 to highest (9 to 13% of CO_2 solubility) in Micromodel #3. The low dsCO_2 concentration in the heterogeneous micromodel implies that under the same groundwater velocity, it may take longer residence time (or water flow path length) in a heterogeneous formation for scCO_2-water to reach equilibrium dissolution than that in a homogeneous one.

The diagram between relative dissolved concentration and $logC_a$ was developed by using the average and range of relative concentrations in each of the 13 experiments and in published core and micromodel experiments. The diagram shows that the concentration of dissolved non-wetting phase fluids (e.g., dsCO_2) increases with the decreasing capillary number, and approaches solubility at low C_a value with sufficient residence time. This main trend is similar to a CDC in a bypass-dominated displacement. Spatially, dissolution of residual CO_2 initiates along the boundary of the bypassed CO_2 cluster(s) in a non-equilibrium manner, and the dsCO_2 concentration in water decreases with increasing C_a and Pe. The main trend is secondarily affected by the coupled dissolution and water flow at localities that fragment the bypassed scCO_2 clusters and enhance scCO_2 dissolution at the pore scale.

For a reservoir-scale scCO_2 plume after cessation of injection, residual CO_2

trapping may be dominated by capillary snap-off as ambient groundwater flow rate is relatively slow (C_a<10^{-7}). The long residence time favors local dissolution and coupled with water flow to approach near equilibrium dissolution. On the other hand, due to the heterogeneous nature of reservoir formations, drainage and imbibition may focus flow in high-permeability channels, and fast dissolution of residual CO_2 into flowing water can be expected. For a $scCO_2$ plume in those low-permeability regions, dissolution is expected to be a lengthy process because of limited interfacial area between mobile water and immobile $scCO_2$. Coupling of water flow and dissolution at localities may occur after the completion of main imbibition in the high-permeability channels, and shorten the dissolution process to some extent. In summary, the reservoir-scale dissolution will be collectively affected by slow ambient groundwater flow and strongly heterogeneity-controlled interfacial areas between groundwater flow and the $scCO_2$ plume.

Acknowledgements

This material was based upon the work supported by the U.S. Department of Energy, Office of Science, Office of Basic Energy Sciences, Energy Frontier Research Centers program under Contract No. DE-AC02-05CH11231. The first author was also supported by the National Natural Science Foundation of China (Grant Nos. 51704297, 51674251), and the China Postdoctoral Science Foundation (2017T100115). The micromodel experiments were conducted at the William R. Wiley Environmental Molecular Sciences Laboratory (EMSL), a scientific user

facility of the U.S. Department of Energy's Office of Biological and Environmental Research operated by the Pacific Northwest National Laboratory (PNNL).

References

Akbarabadi, M., Piri, M., 2013. Relative permeability hysteresis and capillary trapping characteristics of supercritical CO_2/brine systems: An experimental study at reservoir conditions. Adv. Water Resour. 52, 190-196.

Armstrong, R.T., Georgiadis, A., Ott, H., Klemin, Denis, Berg, S., 2014. Critical capillary number: Desaturation studied with fast X-ray computed microtomography. Geophys. Res. Lett. 41, 55-60.

Berg, S., Oedai, S., Ott, H., 2013. Displacement and mass transfer between saturated and unsaturated CO_2-brine systems in sandstone. Int. J. Greenhouse Gas Control 12, 478−492.

Biswas, R.; Lewis, J.E.; Maroncelli, M., 1999. Electronic spectral shifts, reorganization energies, and local density augmentation of coumarin 153 in supercritical solvents. Chem. Phys. Lett., 310 (5-6), 485−494.

Buchgraber, M., Kovscek, A.R., Castanier, L.M., 2012. A study of microscale gas trapping using etched silicon micromodels. Transp. Porous Med. 95, 647−668.

Cadogan, S.P., Maitland, G.C., Martin Trusler J. P., 2014. Diffusion Coefficients of CO_2 and N_2 in Water at Temperatures between 298.15 K and 423.15 K at Pressures up to 45 MPa. J. Chem. Eng. Data 59, 519−525.

Castro A.R., Shokri, N., Karadimitriou, N., Oostrom, M., Joekar-Niasar, V., 2015. Experimental study on nonmonotonicity of Capillary Desaturation Curves in a 2-D pore network. Water Resour. Res. 51, 8517–8528.

Chang, C., Zhou, Q., Xia, L., Li, X., Yu, Q., 2013. Dynamic displacement and

non-equilibrium dissolution of supercritical CO_2 in low permeability sandstone: An experimental study. Int. J. Greenhouse Gas Control 14, 1−14.

Chang, C., Zhou, Q., Guo, J., Yu, Q., 2014. Supercritical CO_2 dissolution and mass transfer in low-permeability sandstone: Effect of concentration difference in water-flood experiments. Int. J. Greenhouse Gas Control 28, 328−342.

Chang, C., Zhou, Q., Kneafsey, T. J., Oostrom, M., Wietsma, T.M., Yu, Q., 2016. Pore-scale supercritical CO_2 dissolution and mass transfer under imbibition conditions. Adv. Water Resour. 92, 142–158.

Chaudhary, K., Cardenas, M.B., Wolfe, W.W., Maisano, J. A., Ketcham, R. A., Bennett, P.C., 2013. Pore-scale trapping of supercritical CO_2 and the role of grain wettability and shape, Geophys. Res. Lett. 40, 3878–3882.

Chomsurin, C., Werth, C.J., 2003. Analysis of pore-scale nonaqueous phase liquid dissolution in etched silicon pore networks. Water Resour. Res. 39 (9), doi:10 1029/2002WR001643.

Chiquet, P., Daridon, J.L., Broseta, D., Thibeau, S., 2007. CO_2/water interfacial tensions under pressure and temperature conditions of CO_2 geological storage. Energy Convers. Manag. 48, 736–744.

Haese, R.R., LaForce, T., Boreham, C., Ennis-King, J., Freifeld, B.M., Paterson, L., Schacht, U., 2013. Determining residual CO_2 saturation through a dissolution test-Results from the CO_2CRC Otway Project. Energy Procedia 37, 5379−5386.

Hildebrand, T., Rüesgsegger, P., 1996. A new method for the model-independent assessment of thickness in three-dimensional images. J. of Microscopy 185,

67−75.

Hilfer, R., Øren, P.E., 1996. Dimensional analysis of pore scale and field scale immiscible displacement. Transp. Porous Med. 22, 53-72.

Hughes, R.G., Blunt, M.J., 2000. Pore scale modeling of rate effects in imbibition. Transp. Porous Med. 40, 295–322.

Hu, R., Wan, J., Kim, Y., Tokunaga, T.K., 2017. Wettability impact on supercritical CO_2 capillary trapping: Pore-scale visualization and quantification, Water Resour. Res., 53, 6377–6394.

Hu, R., Wan, J., Yang, Z., Chen, Y., Tokunaga, T.K., 2018. Wettability and Flow Rate Impacts on Immiscible Displacement: A Theoretical Model. Geophys. Res. Lett. 45, 3077–3086.

IPCC, 2005. Special report on carbon dioxide capture and storage. In: Metz, B., Davidson, O., de Coninck, H.C., Loos, M., Meyer, L.A. (Eds.), Prepared by Working Group III of the Intergovernmental Panel on Climate Change. Cambridge Univer- sity Press, Cambridge, United Kingdom and New York, NY, USA.

Lenormand, R.; Touboul, E.; Zarcone, C., 1988. Numerical models and experiments on immiscible displacements in porous media. J. Fluid Mech. 189, 165–187.

Sahimi, M., 1993. Flow phenomena in rocks—From continuum models to fractals, percolation, cellular automata, and simulated annealing. Rev. Mod. Phys. 65(4), 1393–1534.

Nambi, I.M., Powers, S.E., 2000. NAPL dissolution in heterogeneous systems: An experimental investigation in a simple heterogeneous system. J. Contam. Hydrol.

44(2), 161−184.

Nguyen, V.H., Sheppard, A.P., Knackstedt, M.A., Pinczewski, W.V., 2006. The effect of displacement rate on imbibition relative permeability and residual saturation. J. Petro. Sci. Eng. 52 (1–4), 54-70.

Paterson, L., Boreham, C., Bunch, M., Dance, T., Ennis-King, J., Freifeld, B., Haese, R., Jenkins, C., LaForce, T., Raab, M., Singh, R., Stalker, L., Zhang, Y., 2013. Overview of the CO_2CRC Otway residual saturation and dissolution test. Energy Procedia 37, 6140−6148.

Rasband, W.S., 1997-2018. ImageJ, U. S. National Institutes of Health, Bethesda, Maryland, USA, https://imagej.nih.gov/ij/.

Senel, O., Will, R., Butsch, R.J., 2014. Integrated reservoir modeling at the Illinois basin – Decatur project. Greenhouse Gases Science & Technology 4(5): 662–684.

Spycher, N., Pruess, K., 2005. CO_2–H_2O mixtures in the geological sequestration of CO_2. II. Partitioning in chloride brines at 12–100 °C and up to 600 bar. Geochim Cosmochim AC 69 (13), 3309–3320.

Wang, Y., Zhang, C., Wei, N., Oostrom, M., Wietsma, T. W., Li, X., Bonneville, A., 2012. Experimental study of crossover from capillary to viscous fingering for supercritical CO_2–water displacement in a homogeneous pore network. Environ. Sci. Technol. 47, 212−218.

White, F.M., 1979. Fluid Mechanics. New York: McGraw-Hill, Chapter 6.

Willingham, T.W., Werth, C.J., Valocchi, AJ., 2008. Evaluation of the effects of porous media structure on mixing-controlled reactions using pore-scale modeling

and micromodel experiments. Environ. Sci. Technol. 42 (9), 3185−3193.

Zacharoudiou, I., Chapman, E.M., , Edo S. Boek, E.S., Crawshaw, J.P., 2017. Pore-filling events in single junction micro-models with corresponding lattice Boltzmann simulations. J. Fluid Mech. 824, 550–573.

Zhang, C., Werth, C.J., Webb, A.G., 2002. A magnetic resonance imaging study of dense nonaqueous phase liquid dissolution from angular porous media. Environ. Sci. Technol. 36 (15), 3310–3317.

Zhang, C., Oostrom, M., Grate, J.W., Wietsma, T.W., Warner, M.G., 2011. Liquid CO_2 displacement of water in a dual-permeability pore network micromodel. Environ. Sci. Technol. 45 (17), 7581-7588.

Zhao, B., MacMinn, C.W., Juanes, R., 2016.Wettability control on multiphase flow in patterned microfluidics. Proc. Natl. Acad. Sci. U.S.A. 113 (37), 10251-10256.

Zhao, W., Ioannidis, M.A., 2003. Pore network simulation of the dissolution of a single-component wetting nonaqueous phase liquid. Water Resour. Res. 39 (10), doi:10.1029/2002WR001861.

Zuo, L., Zhang, C., Falta, R.W., Benson, S.M., 2013. Micromodel investigations of CO_2 exsolution from carbonated water in sedimentary rocks. Adv. Water Resour. 53, 188–197.

List of Figures

Figure 1. Pore characteristics of the four micromodels used in this study, with silicon posts in black and pore space in white. The sandstone-analog Micromodel #4 consists of nine identical sub images in a 3 × 3 array, marked by the red dash lines. The blue arrow indicates the water flow direction during imbibition and dissolution experiments. The magnified images for Micromodel #2 and #3 are not to scale.

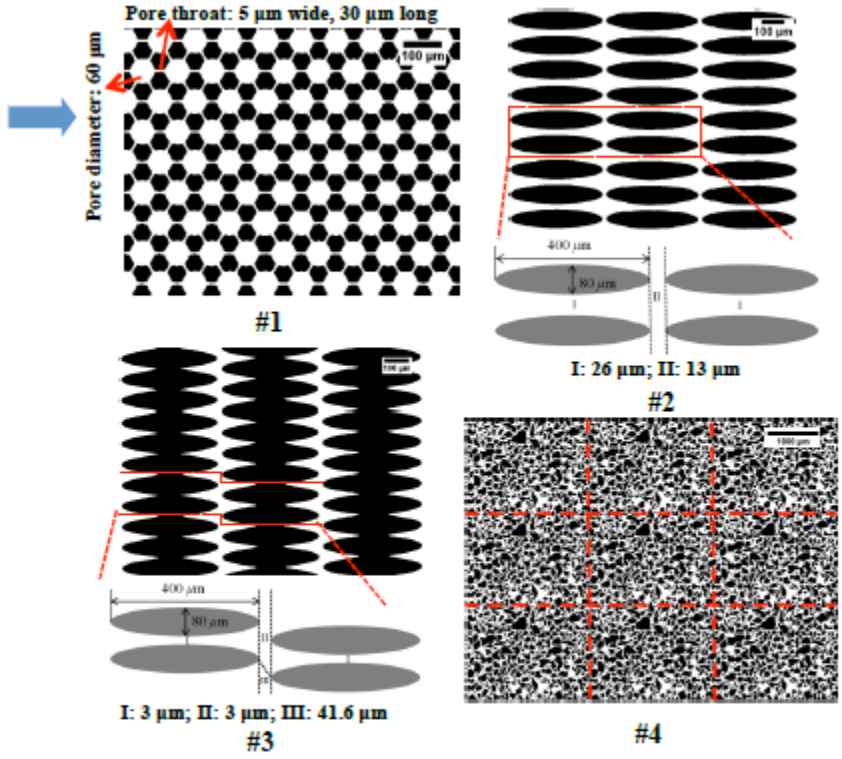

Figure 1

Figure 2. Time-lapse images of $scCO_2$ phase (green) at different times for water imbibition experiments at $logC_a$=−6.53 (a) and −6.13 (b) in Micromodel #1. Water flow is from left to right. The white arrows in (a) indicate the water clusters distributed near the inlet before and after water injection. C1-C5 in (b) marks the five water flow paths developed after imbibition. The white, red and blue boxes indicate the regions magnified to show the competitions between flow paths in Figure 6.

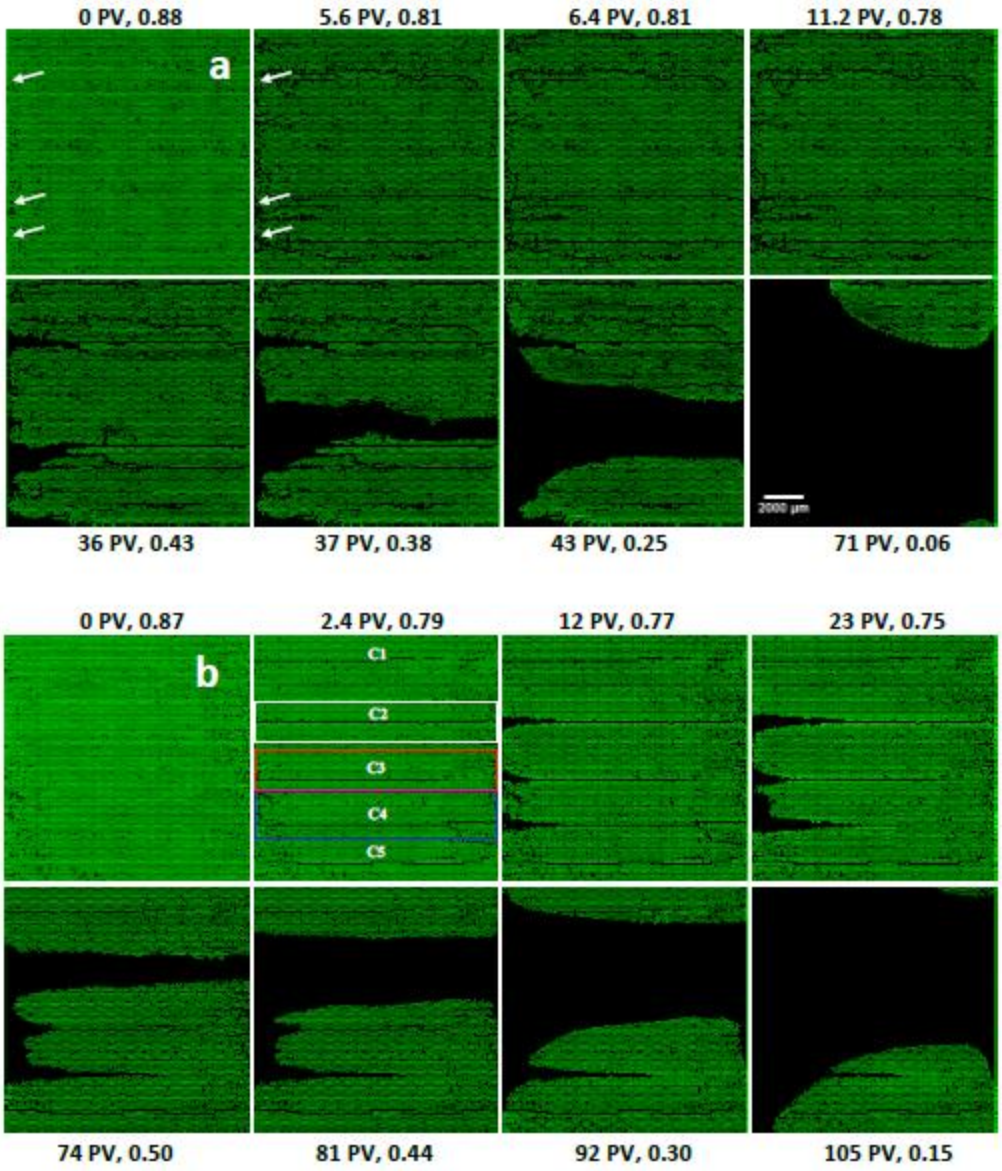

Figure 2

Figure 3. Temporal change in CO_2 saturation, dsCO_2 concentration vs. water injection volume and CO_2 depletion rate vs. CO_2 saturation for imbibition and dissolution experiments at $logC_a$=−6.53 (a-c) and $logC_a$=−6.13 (d-f) in Micromodel #1. The hollow symbols in (a) and (d) indicate the data points at residual CO_2 saturation.

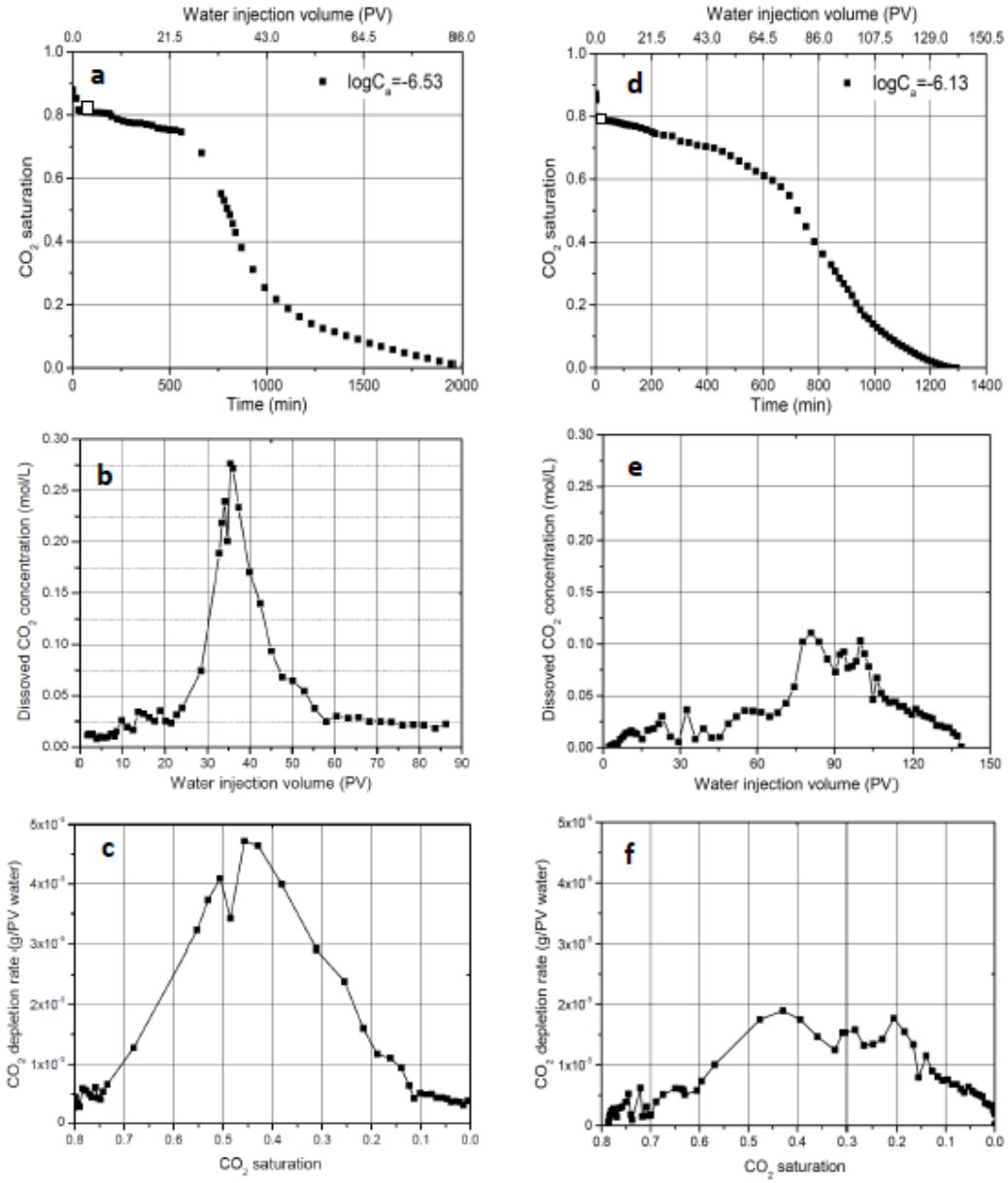
a
logC$_a$=-6.53
Water injection volume (PV)
CO$_2$ saturation
Time (min)
d
logC$_a$=-6.13
b
Dissoved CO$_2$ concentration (mol/L)
e
c
CO$_2$ depletion rate (g/PV water)
f

Figure 3

Figure 4. Dynamic dissolution and depletion of the residual $scCO_2$ at different time intervals and water injection volumes (PV), marked by different colors, during imbibition and dissolution experiments at $logC_a$=−6.53 in Micromodel #1. Water flow paths developed during imbibition are shown in black. The white dotted lines indicate the boundaries of the two large $scCO_2$ clusters at different times. The white arrows indicate the newly created water flow paths at localities.

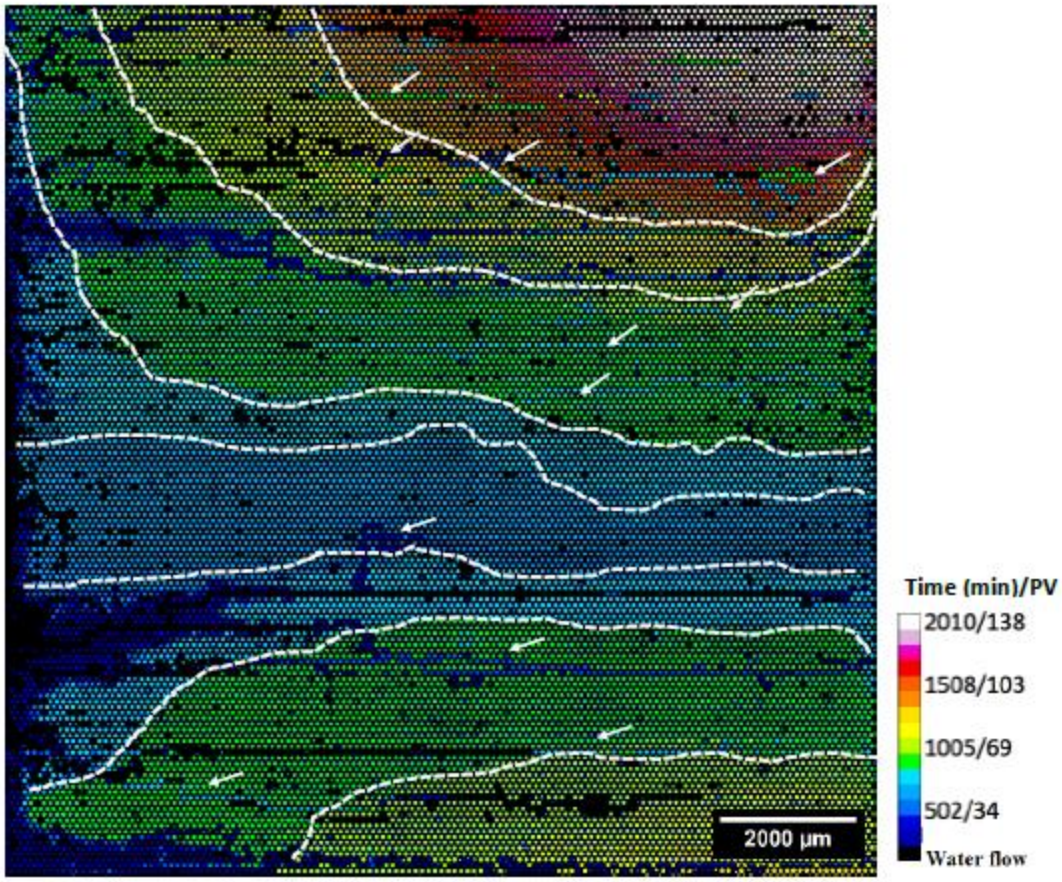

Figure 4

Figure 5. Magnified local regions (with ~30 pores wide) showing the dissolution and depletion of residual $scCO_2$ along the water flow paths #C2 (a), #C3 (b) and #C4 (c) at different time intervals and water injection volumes (PV) marked by different colors, during the imbibition and dissolution experiment at $logC_a$ =−6.13 in Micromodel #1. (d) Relationship of CO_2 saturation vs. time along the five water flow paths at ~30 pore width regions. The red arrow in (b) points to the stable $scCO_2$ bubbles within the narrow flow path and the white arrows in (c) point to the displaced $scCO_2$ cluster (in yellow) within flow path #C4.

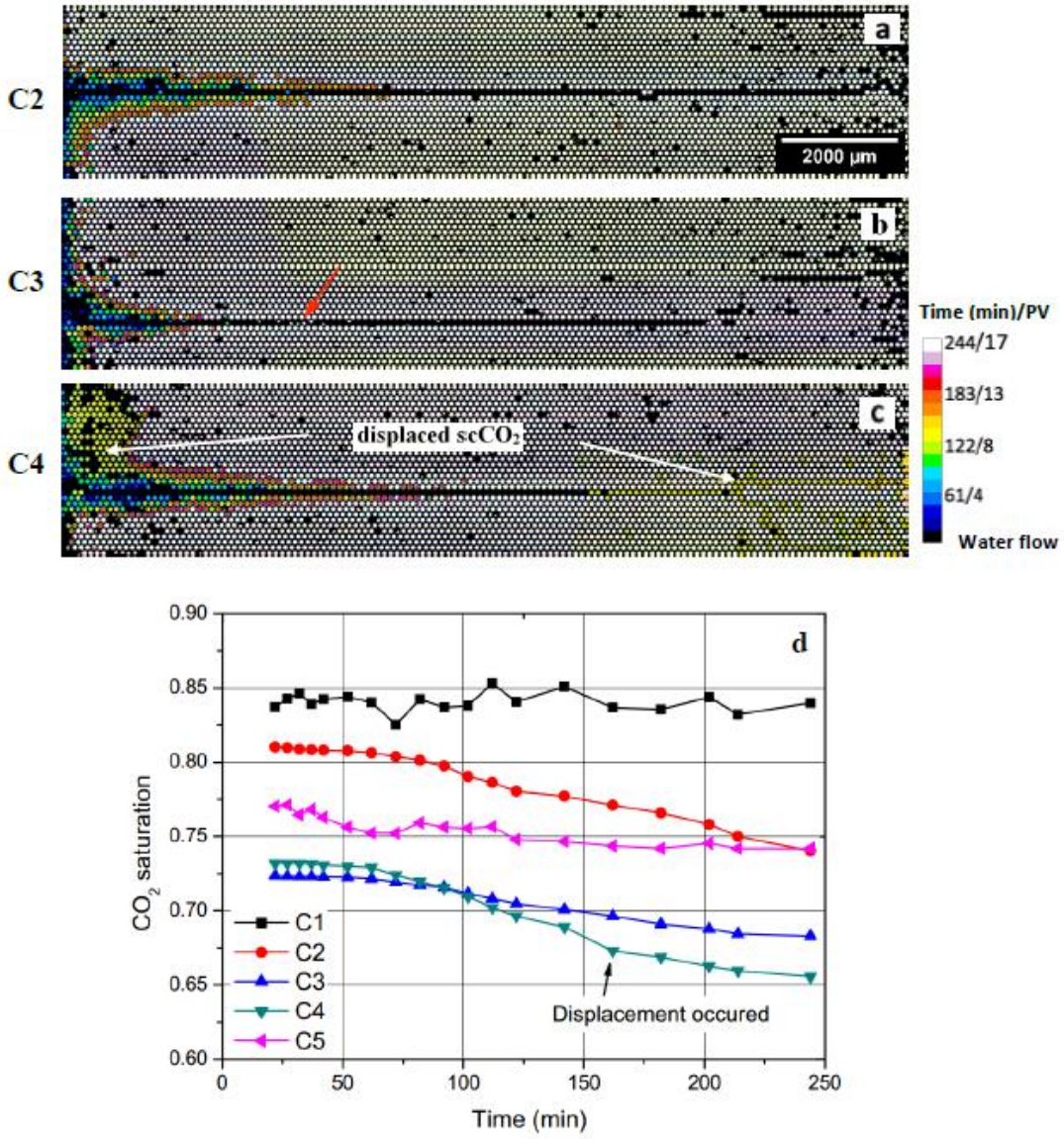
C2
C3
C4
a
2000 μm
b
c
displaced scCO2
Time (min)/PV
244/17
183/13
122/8
61/4
Water flow
d
CO2 saturation
0.90
0.85
0.80
0.75
0.70
0.65
0.60
C1
C2
C3
C4
C5
Displacement occured
0
50
100
150
200
250
Time (min)

Figure 5

Figure 6. Dynamic dissolution and depletion of residual $scCO_2$ at different time intervals and water injection volumes (PV), marked by different colors, during imbibition and dissolution experiment at $logC_a$=−6.13 in Micromodel #1. Water flow paths developed during imbibition are shown in black.

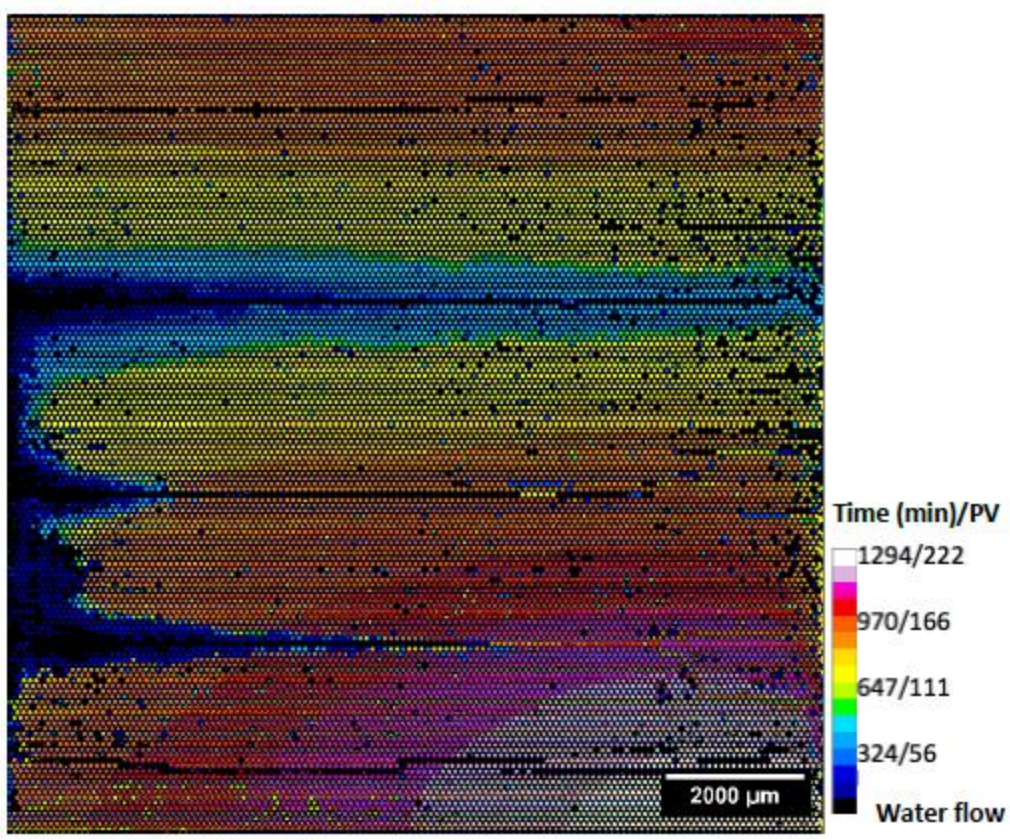

Figure 6

Figure 7. Time-lapse images of $scCO_2$ phase (green) at different times during imbibition with CO_2-saturated water at $logC_a$=−6.13 in Micromodel #1. Water flow is from left to right.

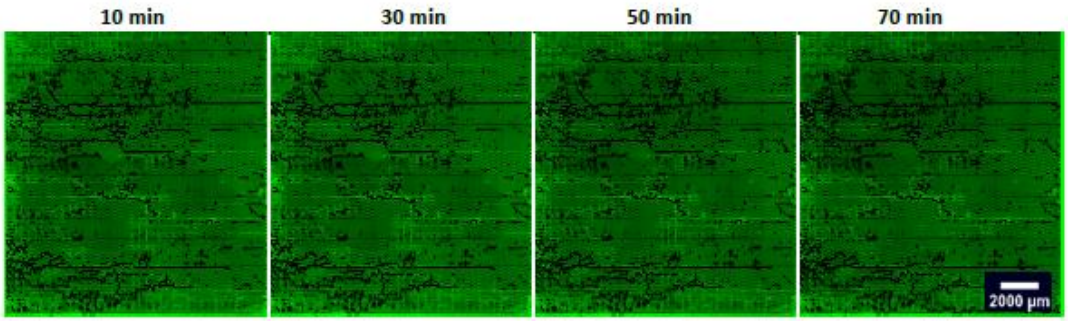

Figure 7

Figure 8. Time-lapse images of $scCO_2$ phase (green) at different times for imbibition and dissolution experiments in Micromodel #1 at (a) $logC_a$=−5.83 (b) $logC_a$=−5.53 and (c) $logC_a$=−5.23. Water flow is from left to right.

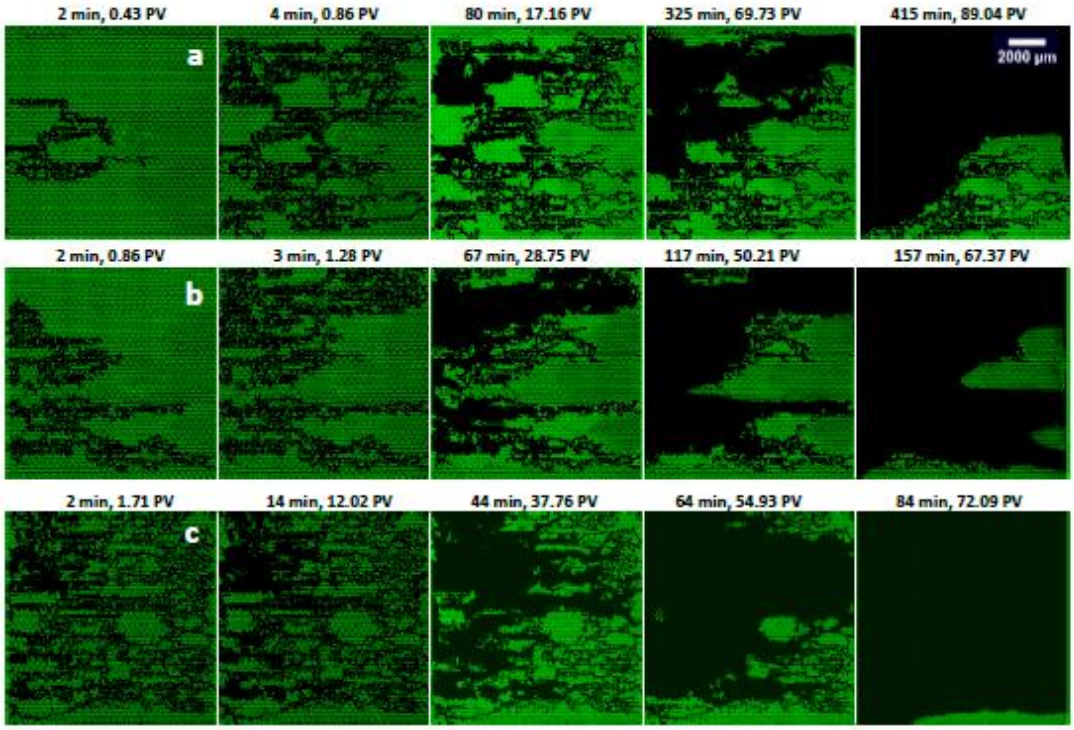

Figure 8

Figure 9. Dynamic dissolution and depletion of the residual $scCO_2$ at different time intervals and water injection volumes (PV) marked by different colors, during imbibition and dissolution experiments at $logC_a$=−5.83 (a), −5.53 (b) and −5.23 (c) in Micromodel #1. Water flow paths developed during imbibition are shown in black. The white arrows indicate the newly created water flow paths.

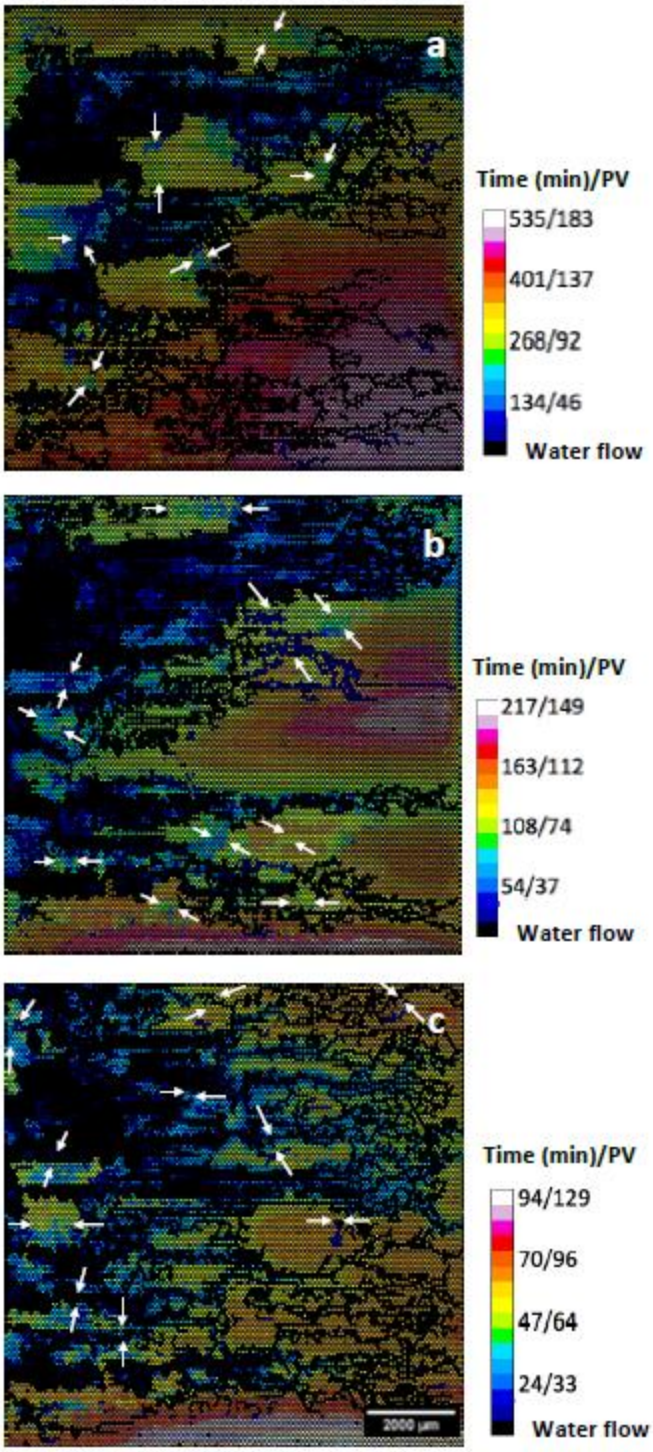
a
Time (min)/PV
535/183
401/137
268/92
134/46
Water flow
b
Time (min)/PV
217/149
163/112
108/74
54/37
Water flow
c
Time (min)/PV
94/129
70/96
47/64
24/33
Water flow
2000 µm

Figure 9

Figure 10. (a) CO_2 saturation vs. time, (b) dsCO_2 concentration vs. water injection volume, and (c) CO_2 depletion rate vs. CO_2 saturation for the imbibition and dissolution experiments conducted in Micromodel #1. The hollow symbols in (a) indicate the data points at residual CO_2 saturation.

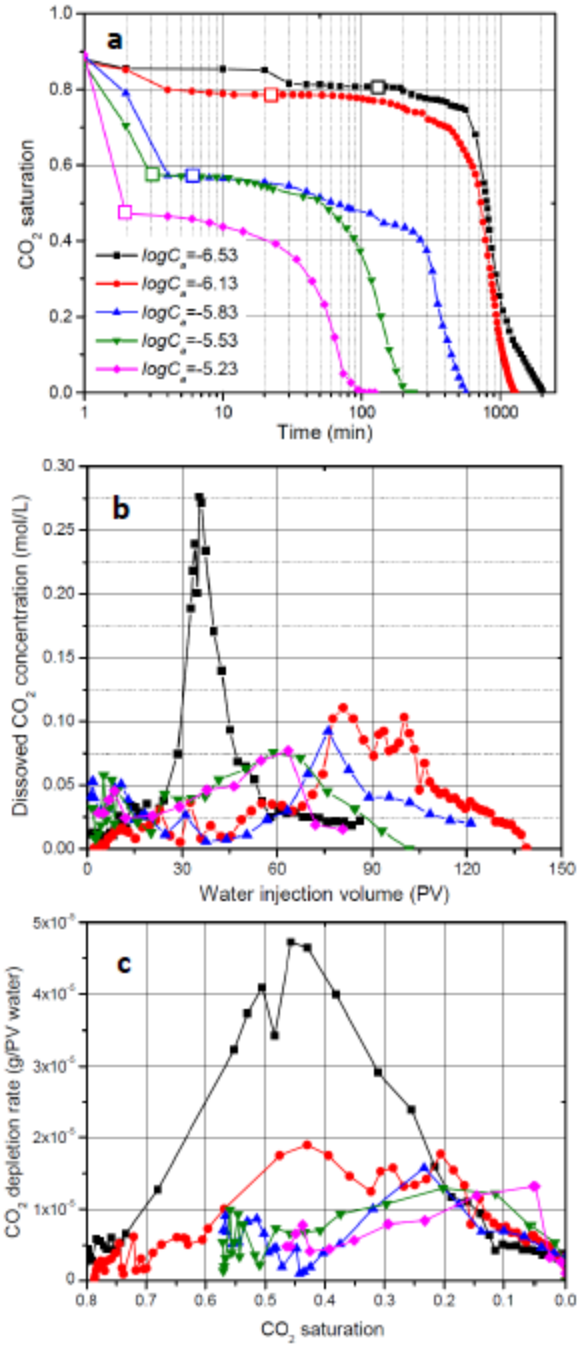
a
CO2 saturation
Time (min)
logCa=-6.53
logCa=-6.13
logCa=-5.83
logCa=-5.53
logCa=-5.23
b
Dissoved CO2 concentration (mol/L)
Water injection volume (PV)
c
CO2 depletion rate (g/PV water)
CO2 saturation

Figure 10

Figure 11. Time-lapse images of $scCO_2$ phase (green) at different times for imbibition and dissolution experiments conducted in Micromodel #2 at $logC_a$=−6.56 (a) and $logC_a$=−5.86 (b). Water flow is from left to right. The associated temporal change in CO_2 saturation, $dsCO_2$ concentration vs. water injection volume, and CO_2 depletion rate vs. CO_2 saturation are shown in (c)-(e), respectively. The white dotted lines in (a) and (b) show boundaries of water-flow paths and $scCO_2$-filled clusters. The white arrows indicate the merger of displacing water with residual water clusters in (a) and several flow paths merge into a larger one in (b) as $scCO_2$ dissolved.

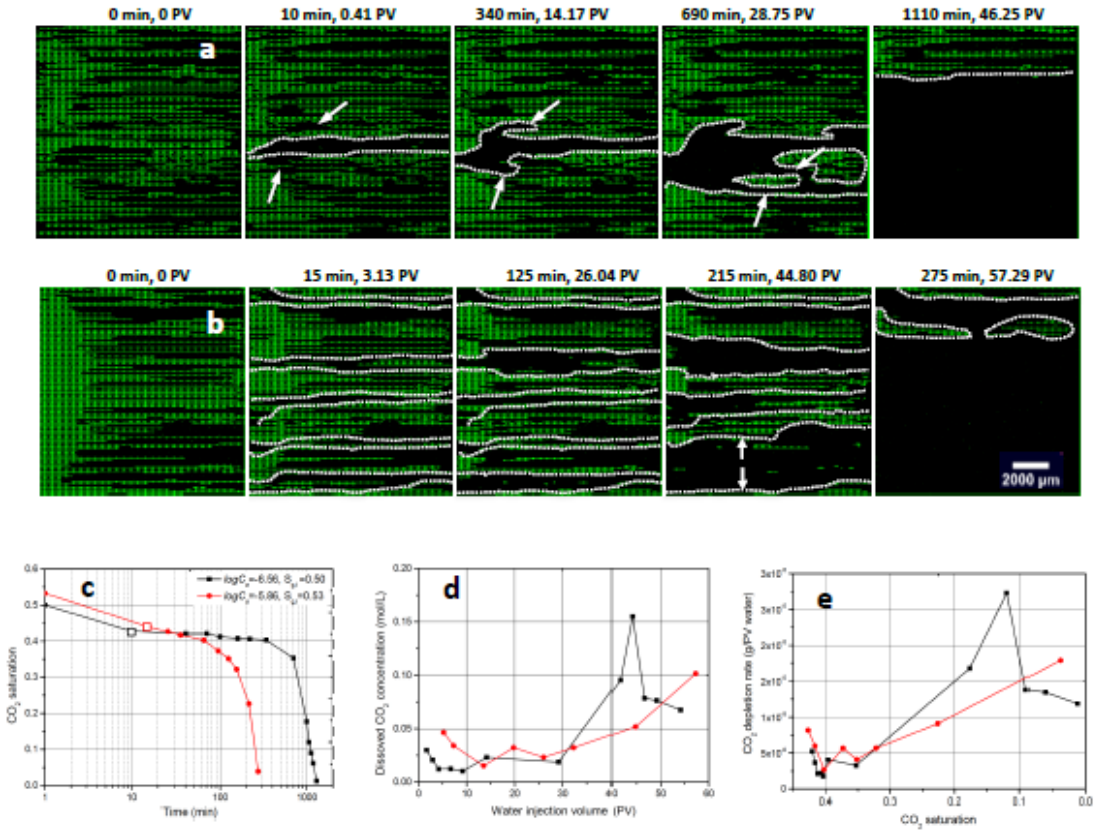

Figure 11

Figure 12. Time-lapse images of $scCO_2$ phase (green) at different times for imbibition and dissolution experiments in Micromodel #3 at $logC_a$=−6.27 (a) and −5.58 (b). Water flow is from left to right. The associated temporal change in CO_2 saturation, $dsCO_2$ concentration vs. water injection volume, and CO_2 depletion rate vs. CO_2 saturation are shown in (c)-(e), respectively. The hollow symbols in (c) indicate the data points at residual CO_2 saturation.

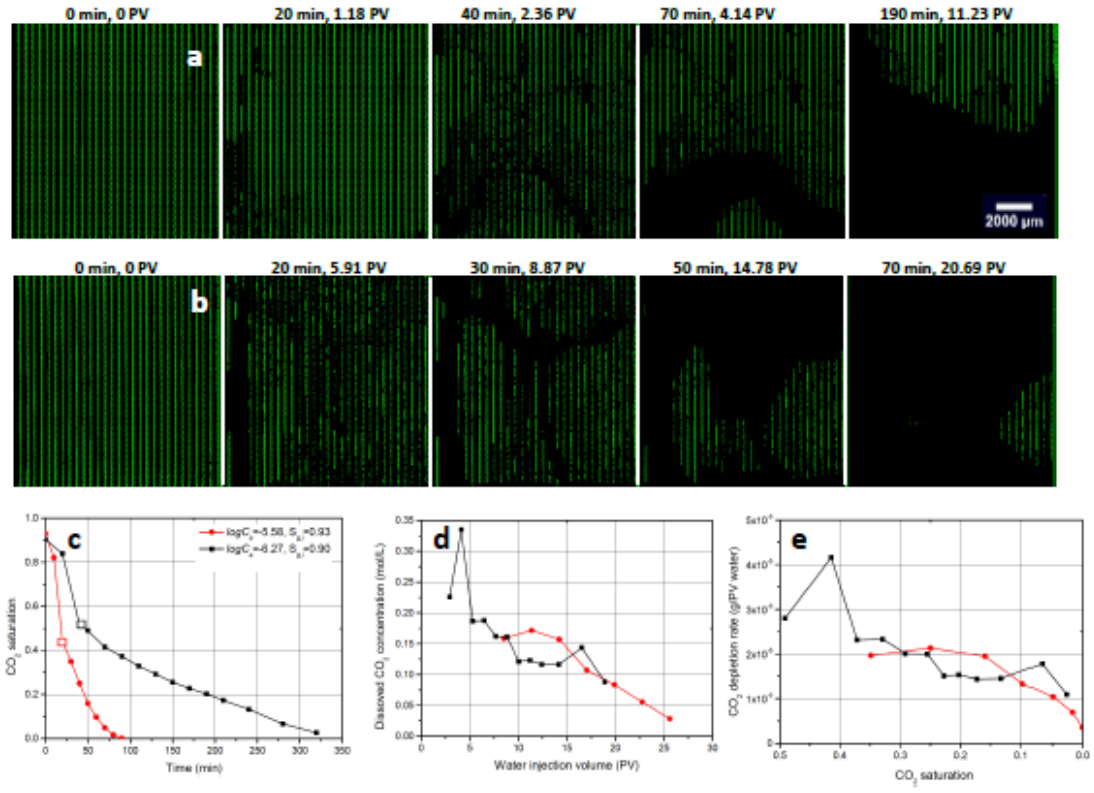

Figure 12

Figure 13. A schematic image showing the residual $scCO_2$ distribution after water imbibition at $logC_a = -4.34$ in Micromodel #4. The silicon posts are shown in blue, water in black and $scCO_2$ in purple. The injected mobile water focuses within the high-permeability channels and bypass the majority of pore-network domain, where CO_2 was trapped and the residual water after drainage was stagnant. The water flow direction is marked by the white arrows and the red arrow indicates the mobile water during imbibition and stagnant water after drainage. The clusters marked by the white dotted lines were used to calculate the cluster-based capillary number. The residual $scCO_2$ distribution for other imbibition experiments in this micromodel can be seen in the supporting information and Chang et al. (2016).

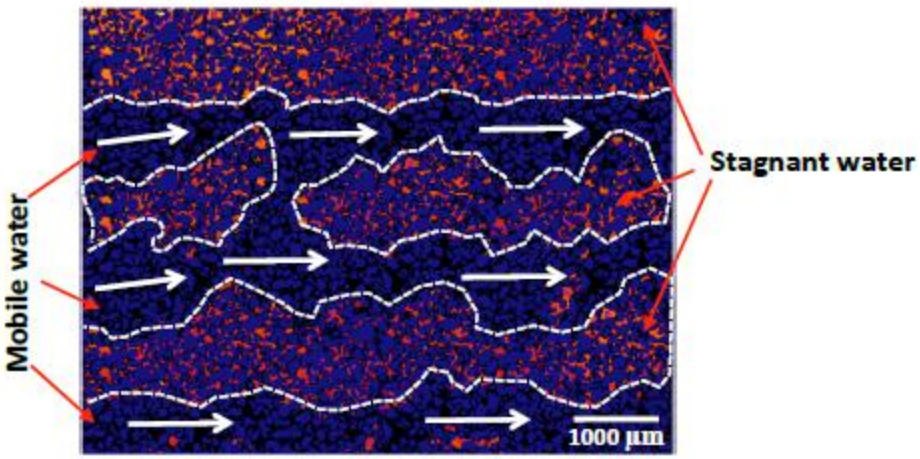

Figure 13

Figure **14**. (a) Residual CO_2 saturation and (b) dissolved CO_2 concentration vs. capillary number C_a for the imbibition and dissolution experiments conducted in the four micromodels. (c) Residual CO_2 saturation vs. the cluster-based capillary number $\overline{C_a}$ in each experiment.

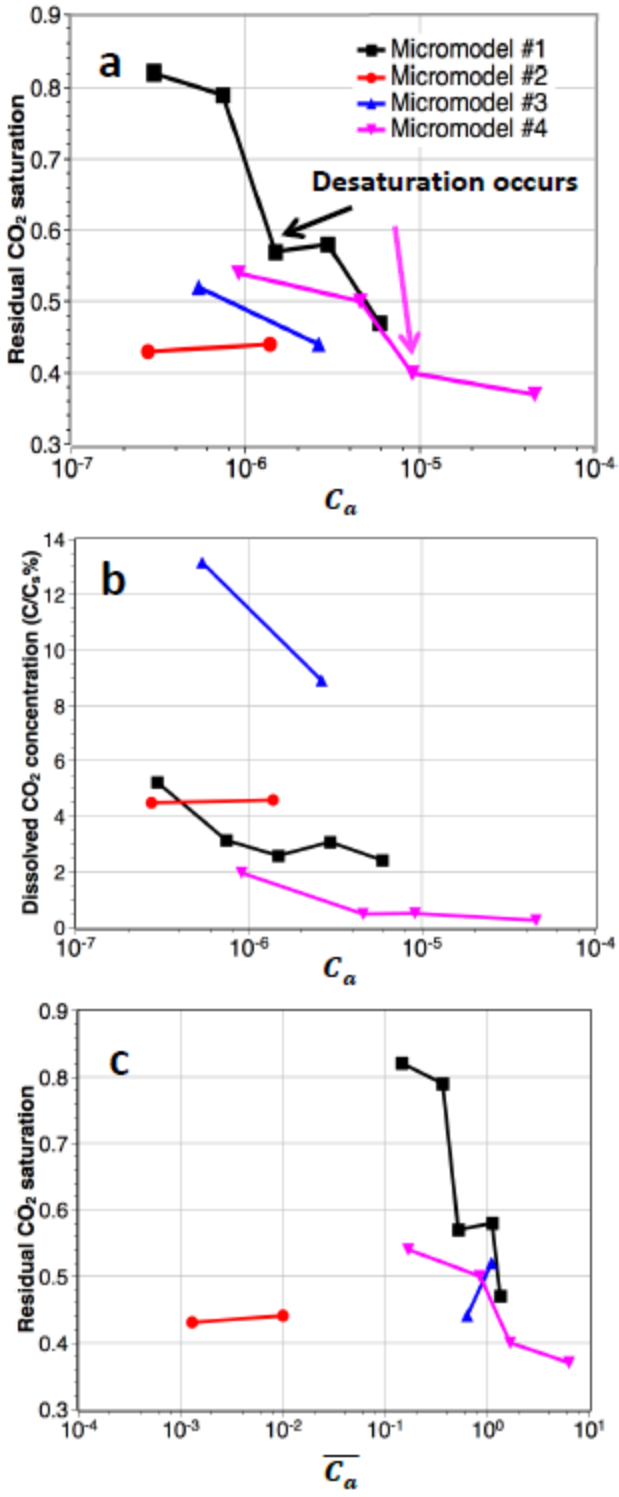
a
Micromodel #1
Micromodel #2
Micromodel #3
Micromodel #4
Desaturation occurs
Residual CO2 saturation
0.9
0.8
0.7
0.6
0.5
0.4
0.3
10-7
10-6
10-5
10-4
Ca
b
Dissolved CO2 concentration (C/Cs%)
14
12
10
8
6
4
2
0
10-7
10-6
10-5
10-4
Ca
c
Residual CO2 saturation
0.9
0.8
0.7
0.6
0.5
0.4
0.3
10-4
10-3
10-2
10-1
100
101
Ca

Figure 14

Figure 15. Dissolved CO_2 concentration as a function of (a) Peclet number Pe and (b) Reynold number Re for the imbibition and dissolution experiments conducted in the four micromodels.

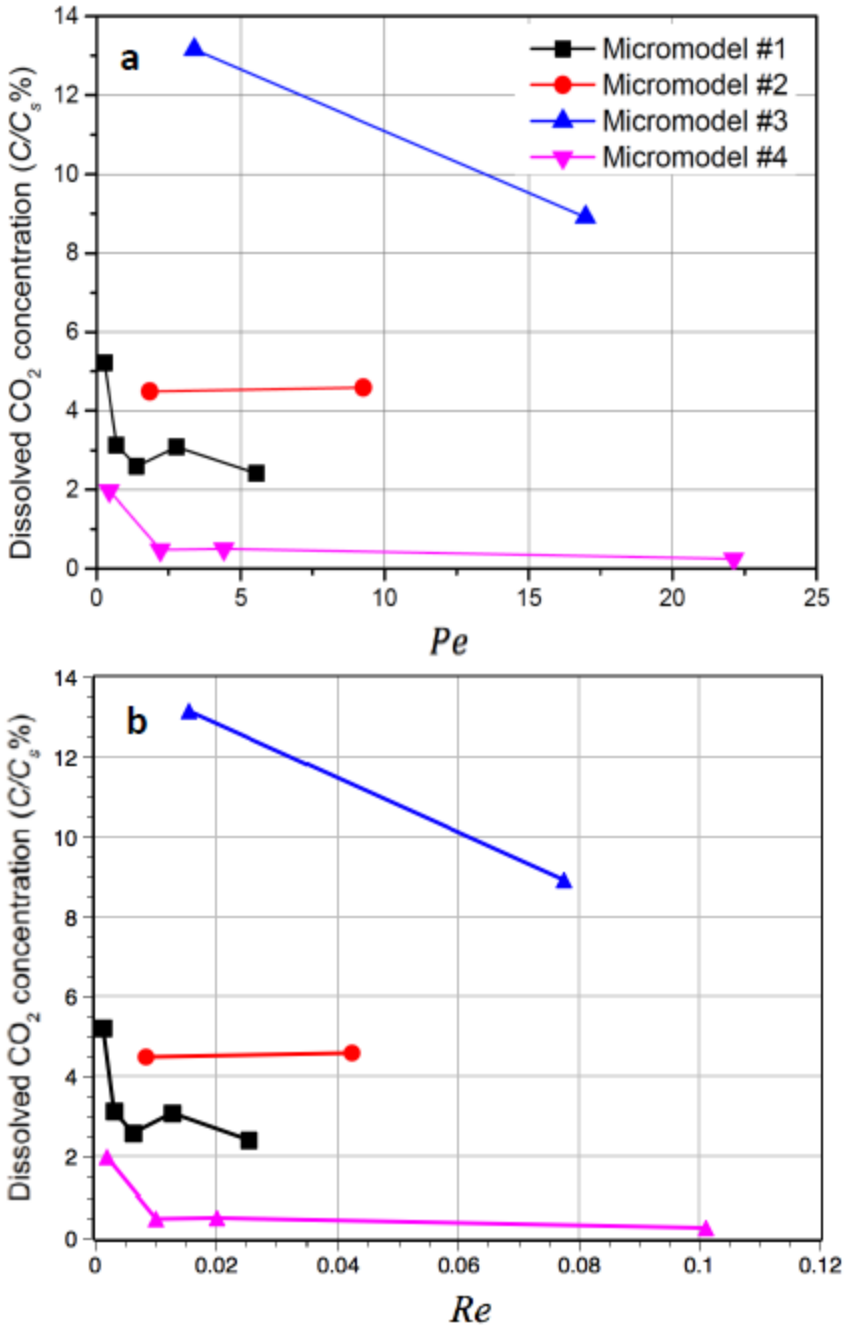

Figure 15

Figure 16. Dissolved phase concentration vs. $logC_a$ for the imbibition and dissolution experiments conducted in the four micromodels in this study, and in two different micromodels by Chomsurin and Werth (2003), in rock cores by Berg et al. (2013) and Chang et al. (2014). The red color bars indicate experiments where the dissolved phase concentration decreased monotonically with decreasing residual phase saturation. The black color bars indicate experiments where non-monotonic change was observed for the dissolved phase concentration vs. residual saturation, when coupled CO_2 dissolution and water flow occur. Zones I (in red) and II (in green) are partitioned by the horizontal dashed line at a relative concentration of 5% and a vertical one at $logC_a$ of -5.20. The horizontal dashed line at a relative concentration of 2% separates the relative concentration in the heterogeneous micromodel from the other micromodels and cores.

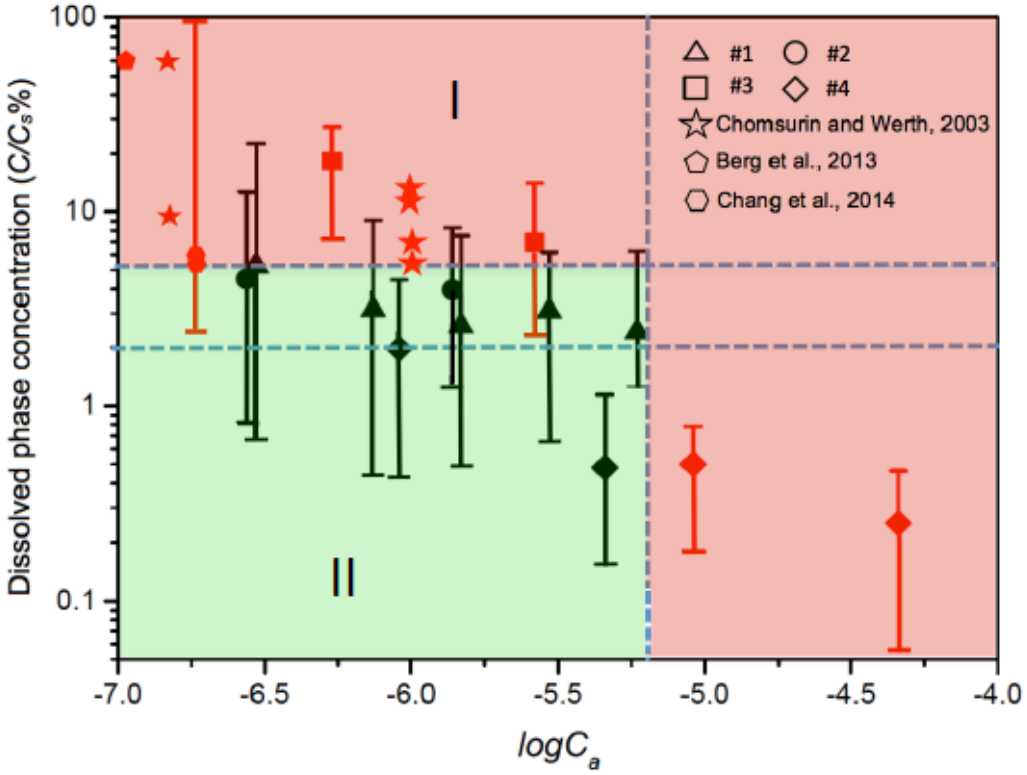
100
10
1
0.1
Dissolved phase concentration (C/Cs%)
-7.0
-6.5
-6.0
-5.5
-5.0
-4.5
-4.0
logCa
I
II
#1
#2
#3
#4
Chomsurin and Werth, 2003
Berg et al., 2013
Chang et al., 2014

Figure 16

Table 1 Micromodel Properties

Micromodel	**#1**	**#2**	**#3**	**#4**
Length×Width (cm×cm)	1.2×1.2	1.2×1.2	1.2×1.2	0.71×0.53
Depth (μm)	37	37	37	35
Porosity	0.44	0.47	0.25	0.35
Permeability (m^2)	6.3×10^{-13}	2.9×10^{-11}	1.1×10^{-13}	7.4×10^{-13}

Table 2 Summary of the imbibition and dissolution experiments conducted in different pore networks

	$S_{g,i}$	Q (μL/h)	$\overline{u}$ (m/d)	$logC_a$	R_e×100	P_e
#1	0.88	10	1.2	−6.53	0.13	0.28
	0.87	25	3.0	−6.13	0.32	0.69
	0.89	50	6.0	−5.83	0.63	1.39
	0.87	100	12.0	−5.53	1.27	2.78
	0.89	200	24.0	−5.23	2.54	5.56
#2	0.50	10	1.2	−6.56	0.85	1.85
	0.53	50	6.0	−5.86	4.23	9.26
#3	0.90	10	2.2	−6.27	1.55	3.40
	0.93	50	11.0	−5.58	7.76	17.00
#4	0.70	10	3.7	−6.04	0.20	0.44
	0.72	50	18.5	−5.34	1.00	2.21
	0.68	100	37.0	−5.04	2.02	4.43
	0.71	500	185.0	−4.34	10.10	22.13

Note: $Re = \rho\overline{u}L/\mu$, $Pe = \overline{u}L/D$, where ρ is water density. The characteristic length scale (L) equals to the median post diameter (Chomsurin and Werth, 2003). For micromodel #1 to #4, L_1=60 μm, L_2=400 μm, L_3=400 μm, L_4=31 μm (Chang et al., 2017). The diffusion coefficient of CO_2 in water (D) was estimated as 3×10^{-9} m^2/s, from Cadogan et al., (2014).

Table 3 Results of the imbibition and dissolution experiments in different pore networks

	$logC_a$	$S_{g,r}$	Imbibition time (min)	Dissolution time (min)	$Q_d \times 10^7$ (g/min)	$C/C_s \times 10^2$	$l^{cl}(cm)$
#1	−6.53	0.82	150	1860	4.69	5.22	1.20
	−6.13	0.79	22	1272	7.04	3.13	1.20
	−5.83	0.57	8	557	11.65	2.59	0.86
	−5.53	0.58	3	235	27.67	3.08	0.91
	−5.23	0.47	2	122	43.38	2.41	0.55
#2	−6.56	0.43	10	1290	4.03	4.49	0.41
	−5.86	0.44	15	260	20.64	4.59	0.63
#3	−6.27	0.52	40	280	11.82	13.16	1.00
	−5.58	0.44	20	70	40.0	8.91	0.12
#4	−6.04	0.54	10	750	1.77	1.97	0.71
	−5.34	0.50	10	575	2.14	0.48	0.71
	−5.04	0.40	10	220	4.48	0.50	0.71
	−4.34	0.37	1.0	70	11.43	0.25	0.53